Influence of cell design and hydrodynamics on performance of redox flow batteries

Master's Thesis

Talitha Giaquinto

Supervisors:

Jens Muff
Sebastian B. Kristensen

Aalborg University Esbjerg
Department of Chemical Engineering
June 2019

Chemical Engineering
Aalborg University
http://www.aau.dk

Title:
Influence of cell design and hydrodynamics on performance of redox flow batteries.

Theme:
Redox flow batteries

Project Period:
Spring semester, 2019

Project Group:
K10K-1-F19

Participant(s):
Talitha Giaquinto

Supervisor(s):
Jens Muff
Sebastian B. Kristensen

Copies: Digital Submission

Page Numbers: 79

Date of Completion:
2019-06-07

Abstract:

Redox flow batteries (RFBs) have emerged as prime candidates for energy storage of fluctuating renewable energy because of their ability to be scaled separately in terms of energy and power and, therefore, to potentially reduce the costs of energy storage. In particular, alkaline flow batteries based on redox-active organic molecules (quinones) and on a solution of a food additive (potassium ferricyanide), have been proven able to deliver a cell potential of 1.2 V. The investigations focused on operating 2,6-dihydroxyanthraquinone and 2,5-dihydroxy-1,4-benzoquinone, whose reduction kinetics were evaluated through means of cyclic voltammetry, to test the performance of a newly acquired redox flow battery presenting a 'zero-gap' cell configuration. Furthermore, studies on the influence of flow and hydrodynamics on the electron transfer were carried out through the limiting-current technique, which was found not to be informative. However, despite the success of the investigations that lead to the choice of 2,6-dihydroxyanthraquinone and 2,5-dihydroxy-1,4-benzoquinone as negolytes, issues occurred during the testing phase of the flow battery.

Preface

The present writing is a Master's Thesis named *Influence of cell design and hydrodynamics on performance of redox flow batteries*. It is a 10th semester project in terms of the *Specialization in Chemical Engineering* module (30 ECTS credits) in Chemical Engineering Master's degree programme at Aalborg Universitet (AAU), Esbjerg. The thesis period lasted from February until June, 2019.

The choice of working on the chemistry of redox flow batteries during the thesis arose from the same concern about environmental preservation that pushed me to move to Denmark two years ago. The thesis period has been an intense and challenging series of ups and downs, during which I have been experiencing joy as much as disappointment. However, I have to admit that never once, during this period, have I felt abandoned by my supervisors.

I hope this writing will be considered as a comprehensible and professional piece of work by whomever audience wishes to read it.

Talitha Giaquinto

Aalborg Universitet, Esbjerg, Denmark

7 June, 2019

Contents

1. Introduction

The production of electricity that meets the Global energy demand is mostly supplied by fossil fuel ($\sim$ 85 % of mankind's primary energy) and nuclear-based power plants [1]. These conventional energy production plants have typical power outputs of over 1 GW, but are far from being sustainable. In fact, burning fossil fuel and biomass produce gaseous emissions that are not only polluting the air but also increasing global warming with an alarming rapidity (the concentration of carbon dioxide in the atmosphere has increased from 280 ppm in 1995 to over 400 ppm in December 2015) [2]. Moreover, the constant energy source provided by nuclear reactors is associated with problems of radioactive waste disposal and a foreign oil and/or gas dependency could create a climate of national vulnerabilities that could threaten social stability [2]. For these reasons, it is worldwide concern to build a low-carbon society supported by sustainable energies, such as solar, wind, geothermal or hydroelectric energy.

Renewable energy sources will provide almost 30 % of the worldwide power demand by 2023, up from 24 % in 2017 [3]. Nevertheless, as geothermal energy and hydroelectricity are globally limited to specific geographic locations because of disadvantages regarding reduced availability (e.g. sunlight in the night [4]) and massive ecological impact, solar and wind intermittent energy seems to be the only environmentally friendly alternative source of electricity [5]. As a matter of fact, solar and wind installed capacities are growing at rates of 60 % and 20 % per year respectively [6], and the goal, in Europe, is to reach 20 % of total electricity production from renewable sources by 2020 and at least 32 % by 2030 [7]. Moreover, worthy of mention is the ability of Denmark to become a leader in renewable energy generation as, measuring electricity supply alone, renewables account for above 50 % of domestic generation, mostly due to the incorporation of wind energy in the electricity production (5 GW of installed wind energy capacity) [8]. Because solar and wind energy production is intermittent, though, energy demand can diverge from energy production [9]; however, conventional power plants produce a stable base load over a long period of time. This means that safe, low-cost, efficient and scalable energy storage technologies, able to overcome deviations in energy production and consumption, are needed.

Currently, a series of storage technologies are available, such as pumped hydro,

fly - wheels, compressed air, supercapacitors, solid-electrode batteries, and redox flow batteries [4]. Among the options for electrochemical storage of renewable energies, redox flow batteries represent a valid alternative to enclosed conventional batteries, which exhibit limited energy-to-power ratios that increase the cost when the required discharge duration exceeds one hour. Moreover, the repeated charge/discharge cycles that conventional batteries undergo determine expansion and contraction of the electrode materials, which results in degradation of the material over time and severely limits the cyclic lifetimes of the battery [10]. Redox flow batteries, instead, present redox-active cathode and anode materials dissolved as electrolytes, stored in external tanks outside the cell itself. This design allows the cycle life of flow batteries not to be dependent on the depth of discharge [10] and a great flexibility of the system, as the power capacity (electrode area) and energy capacity (tank size) can be independently sized so that the discharge duration can be rather inexpensively increased simply by increasing the size of the tanks. Furthermore, the power of flow batteries can be more easily scaled - up than is for conventional batteries, as it is sufficient to increase the active surface area of the electrodes, the number of electrodes in a cell stack and the number of cell stacks in a system [4]. On the other hand, scaling - up of the storage capacity of RFB is achieved by increasing the volume of electrolytes and/or the concentration of active species [4].

1.1 State of the art review

As of today, the most common type of redox - flow batteries technology is the all - vanadium flow batteries (VRFB), first developed in the University of New South Wales by Skyllas-Kazacos and her co-workers in the 1980s. This technology immediately acquired worldwide interest, as it makes use of four different oxidation states of vanadium ions, hence enabling the decrease of cross-transport of the active components in the two half-cells, since one only type of active element is employed in the cell [11]. In this set-up, the two couples VO_2^+/VO^{2+} and V^{2+}/V^{3+} are separated as catholyte active species and anolyte species, respectively, and undergo the following electrode reactions [12]:

Cathode-side:

$$\mathrm{VO_2}^+ + 2\,\mathrm{H}^+ + \mathrm{e}^- \underset{\text{Charge}}{\overset{\text{Discharge}}{\rightleftharpoons}} \mathrm{VO}^{2+} + \mathrm{H_2O} \quad E^o = 1.00\,V \tag{1.1}$$

Anode-side:

$$\mathrm{V^{2+} - e^{-}} \underset{\text{Charge}}{\overset{\text{Discharge}}{\rightleftharpoons}} \mathrm{V^{3+}} \quad E^o = -0.25\,V \tag{1.2}$$

Cell reaction:

$$\mathrm{VO_2{}^{+} + 2\,H^{+} + V^{2+}} \underset{\text{Charge}}{\overset{\text{Discharge}}{\rightleftharpoons}} \mathrm{VO^{2+} + V^{3+} + H_2O} \quad E^o = 1.25\,V \tag{1.3}$$

However, *Sum et al.* [11] state that the performance of VRFB is hindered by the solubility (2.0 - 3,0 M) and the stability of vanadium ions in the electrolyte solutions, which limit the energy density of the VRFB to 20-60 Wh / L [13]. Moreover, as VRFB are confined to work in a temperature range between 10 °C and 40 °C, an active heat management system is needed during operation with the VRB stack, lowering the system efficiency due to parasitic energy losses. According to *Chen et al.* [14]), these problematics, coupled with high cost of vanadium ions (USD$ 300 - 800 (kW h)$^{-1}$, ca. $27/kg), high V(V) corrosiveness and the need for relatively expensive ion exchange membranes, which represents 40 % of the total cost of the battery, have pushed the research towards more sustainable flow battery technologies and, as a matter of fact, latest studies have been focused on developing redox flow batteries that could use organic active materials as electrolytes [4].

The abundance of organic molecules, and the possibility of their extraction from various sources, decrease the electrolyte costs for organic - based flow batteries (USD$ 35 (kW h)$^{-1}$, based on half - cell estimations [15]). This could represent a valid alternative for reducing the overall cost in long-term, to meet the proposed cost target of USD$ 150 (kW h)$^{-1}$ reported by the Office of Electricity in 2013 [16]. Moreover, it is possible to further optimize the properties of the organic molecules to provide faster kinetics and higher solubilities, and to yield high cell voltages in batteries [4]. In this regard, the focus of current studies [17–19] is the optimization of aqueous organic-inorganic redox flow batteries, involving one organic and one inorganic active material for the two electrode reactions, as these have been proven successful in increasing the cell voltages, in decreasing cost and have shown significant advantages in ionic conductivity.

Hazza et al. [20] stated that the most used low-cost inorganic redox couples for organic-inorganic batteries are zinc, bromine and ferricyanide, having shown higher specific energy (e.g., zinc: 820 A h kg^{-1}; bromine (Br_2): 335 A h kg^{-1}) when used in conventional flow batteries. As for the organic redox couples employed, instead, quinones, aromatic compounds containing secondary hydroxyl groups, have been chosen for their high reversibility for energy storage applications. *Leung et al.* [4] specify that, when in aqueous eletctrolytes environment, the hydroxyl groups work

as hydrogen carriers: electrical energy can be released by oxidation of these groups so that the corresponding hydrogen depleted carbonyl compounds can be formed. However, some concerns over the employment of quinones in the organic-inorganic flow battery systems are related to the reversibility of the redox reactions and their solubilities in water. It can happen that the redox reactions might need catalysts or elevated temperatures, such as 150 °C - 250 °C and, in some cases, the dehydrogenation (oxidation) process of these compounds results in slower kinetics compared to the hydrogenation (reduction) process, which is not practical in many redox flow battery applications [4]. *Huskinson et al. (2014)* [19] stated that another important aspect to take into consideration for governing the reactions when employing aqueous electrolytes in redox flow batteries systems, is the pH of the solution, as it has a significant influence on the solubility and chemical stability of the organic molecules.

Lin et al. (2015) [17] have finalized an organic-inorganic redox flow battery based on alkaline electrolytes. The system is formed by 0.5 mol/L 2,6-dihydroxyl anthraquinone *(2,6-DHAQ)* and 0.4 mol/L potassium ferricyanide *(Fe(CN)*$_6^{3-}$), both dissolved in 1 mol/L of potassium hydroxyde and working as the negative and positive electrolytes, respectively. Ferricyanide is preferred to bromine because it is non-toxic (as a matter of fact, it is used as food additive) [21]. In alkaline electrolytes, both the redox active species in both reduced and oxidized states have shown solubilities greater than 0.6 mol dm^{-3}. Investigations of the reduction potentials of the two species made with cyclic voltammogram deliver an open-circuit cell voltage of 1.2 V at 50% state of charge [17]:

Anode reaction:

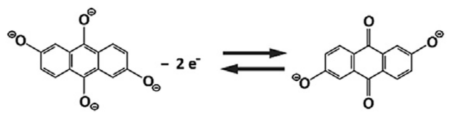

Figure 1.1: 2,6-DHAQ anodic reaction. [17]

and the following half-cell potential:

$$E^o \approx -0.65\,Vvs.SHE \tag{1.4}$$

Cathode reaction:

$$Fe(CN)_6{}^{3-} + e^- \rightleftharpoons Fe(CN)_6^{4-} \quad E^o \approx +0.36\,Vvs.SHE \tag{1.5}$$

Cell cycling was performed at 20 °C in a parallel flow cell, where carbon papers were employed as electrodes and a Nafion®212 cation exchange membrane was used as a separator. After 100 charging/discharging cycles at 100 $mA\,cm^{-2}$, results showed a round trip energy efficiency of 84% with a current efficiency of more than 99%, whilst the capacity loss, to be attributed to the cross-over of the active species across the membrane, to the leakage from the pumping system and to the chemical decomposition, was found out to be 0.1% for each cycle. Moreover, the system was capable of delivering an energy density of ca. 6.8 $W\,h\,dm^{-3}$ and total power density of 4501 mW/cm^2 [17].

More recent studies from *Yang et al. (2017)* [18], have introduced an alkaline redox flow battery that utilizes 0.5 mol/L 2,5-dihydroxy-1,4-benzoquinone (*2,5-DH-1,4-BQ*) dissolved in 2 mol/L potassium hydroxide as the negolyte and 0.4 mol/L potassium ferrocyanide *($K_4Fe(CN)_6$)* dissolved in 1 mol/L potassium hydroxide as the negolyte. In this study, the benzoquinone is preferred to the anthraquinone because substantially less expensive. Through cyclic voltammetry investigations, the open-circuit cell voltage is reported to be 1.21 V at 50% state of charge (SOC). The parallel flow cell is assembled with Nafion ®212, 115 and 117 membranes as separators and carbon papers as electrodes. Through cell cycling, the initial capacity is found to be 23.15 Ah/L and the coulombic efficiency (CE) is 77% when using N212 membrane (self-discharge of the cell due to cross-over of the active species across the membrane) [18].

1.2 Problem statement

According to the aforementioned studies (section 1.1), much has yet to be done in terms of implementing cell performance (cell voltage, current density, coulombic efficiency) and tuning of physical/electrochemical properties (number of electron-transfers, solubility, molar mass) in order for the organic-inorganic flow battery to compete with conventional all-vandium systems, able to achieve energy densities of ca. 35 $W\,h\,dm^{-3}$, cell voltages of 1.5 V, solubility up to 2.0 $mol\,dm^{-3}$ and high specific capacity of vanadium (526 $A\,h\,kg^{-1}$) [4]. In line with the latest studies' developments, the project known as *Fungal flow-battery for storing sustainable energy*, active in the Section of Biotechnology, Department of Chemistry and Bioscience in the Section of Chemical Engineering in the Faculty of Engineering and Science of Aalborg University Esbjerg, aims at developing an all-organic redox flow battery completely based on quinones extracted from filamentous fungi. For this reason, a cell consisting of two Poco graphite plates with serpentine flow field provided from Fuel Cell Technologies (FCT) and a new

battery tester (Neware BTS-5V6A) were bought from the University of Aarhus around December 2018.

The experimental work carried out during this master's thesis period was conceived to be the first step for implementing the electrochemistry part of the above mentioned project, and had the general aim of using the features of the newly acquired battery test station to study the performances of the cell when investigating the cell design. In this perspective, the objectives of this master's thesis can be expressed as follows:

- How to choose the most performing quinones to be operated in the newly acquired cell?
- Is the newly acquired cell properly functioning when redox species flow through it?
- Is it possible to optimize the flow of redox species through the cell by focusing the investigations on the cell design, such as, for example, flow fields, gaskets, electrodes and membranes?
- Will the optimization of the flow through the cell lead to an optimized performance of the battery, such as implemented current efficiencies, capacity and power/current densities?
- In order to get more knowledge about the behaviour of the redox reactions happening during charge and discharge of the cell, is it possible to study the mass transfer coefficient of the chemical species employed in the cell through the limiting-current method and use it to study the influence of flow and flow pattern (hydrodynamics) on the electron transfer?

To answer these questions, a plan of action was designed in accordance with previous studies ([17,18]), which operate organic-inorganic redox flow batteries with petro-quinones. Therefore, by means of cyclic voltammeter, the redox kinetics of a wide selection of petro-quinones available in the laboratory of the Section of Chemical Engineering at Aalborg University Esbjerg were investigated. After the screening, the chosen redox couples (*2,6-DHAQ, 2,5-DH-1,4-BQ and 1,4-NQ*) should have been operated in the new battery setup, and cell cycling tests should have been run in order to get valuable data about the performance of the flow battery (cell potential [V] vs. current density [A cm^{-2}]; cell voltage [V] vs. capacity [C]; efficiency [%] vs. cycle number, cell voltage [V] vs. time [hr]). However, unexpected issues occurred during the trial phase. Hence, the initial goals of the thesis shifted toward new types of investigations, whose core was aimed at answering the one and only following question:

- Why is that, despite the proven functioning redox kinetics of the chemicals employed, the flow battery seems not to work as expected?

This and other questions will be answered later in this piece of work, and the logic behind the choices made will become clear.

2. Background

The following chapter covers the general concept of decentralized energy systems and energy storage technologies. In particular, electrochemical storage systems and its subcategories will be presented, and much importance will be given to redox flow-battery technology. To fully understand the working mechanism of this batteries, the chemical species employed, the kinetics governing the redox reactions and the design of the battery will be introduced.

2.1 Decentralized energy systems

Worldwide urgency to satisfy the ever-increasing demand for electricity consumption and promotion of environmental protection are the main reasons that encouraged electricity production from renewable energy sources [22]. Moreover, the scarcity of fossil fuels and price volatility of oil and gas imports are leading to the disposal of centralized power generations (large fossil fuel condensing plants, or nuclear plants, that transmit generation loads across long transmission and distribution lines to consumers in the region) in favour of cleaner and more agile decentralized energy production systems, characterized by locating of energy production facilities closer to the site of energy consumption [23]. The working conditions set by fossil fuel plants and centralized generation networks on the traditional power grids represent a real challenge for the applicability of renewable energy sources technologies such as wind turbines: fluctuating and/or intermittent wind energy production, owing to wind speed variability, is unable to adjust to the profile of electricity demand [24].

A decentralized energy system has the advantages of higher energy efficiencies, avoidance of transmission and distribution losses, enhanced flexibility of the local electricity network and increased levels or reliability/security of supply. It relies on distributed generation (DG), demand response (DR) and energy storage [24]:

Distributed generation is defined as an electric power generation source connected directly to the distribution network and located close to the load. This allows for the employment of numerous, but small plants and can provide power on-site with little

reliance on the distribution and transmission grid. DG technologies yield power in capacities that range from a fraction of a kilowatt [kW] to about 100 megawatts [MW]. Utility-scale generation units generate power in capacities that often reach beyond 1,000 MW [24].

Demand response accounts for the changes in the price of electricity over time, thereby representing the changes in electric usage by demand-side resources from their normal consumption patterns. This means that real-time monitoring and communication between producers and consumers of electricity is possible, and it helps the optimization of grid usage [25].

Energy storage systems balance supply and demand due to short- and long-term storage duration periods, while aiding in frequency and voltage control at local and large grid scales [26]. For this reason, large-scale energy storage systems (ESSs), able to store energy at off-peak hours and supply energy at peak hours and improve grid stability, are becoming the kernel components of the smart power grids technologies, ensuring a consistent flow of energy [9,27].

2.1.1 Energy storage technologies for renewable energy systems

In order for the energy storage systems (ESSs) to balance demand and supply, the electrical energy needs to be converted from an available source to another, and then converted back into electrical energy when needed. There are 5 main forms of energy storage, as visible in Figure 2.1 [26,28,29].

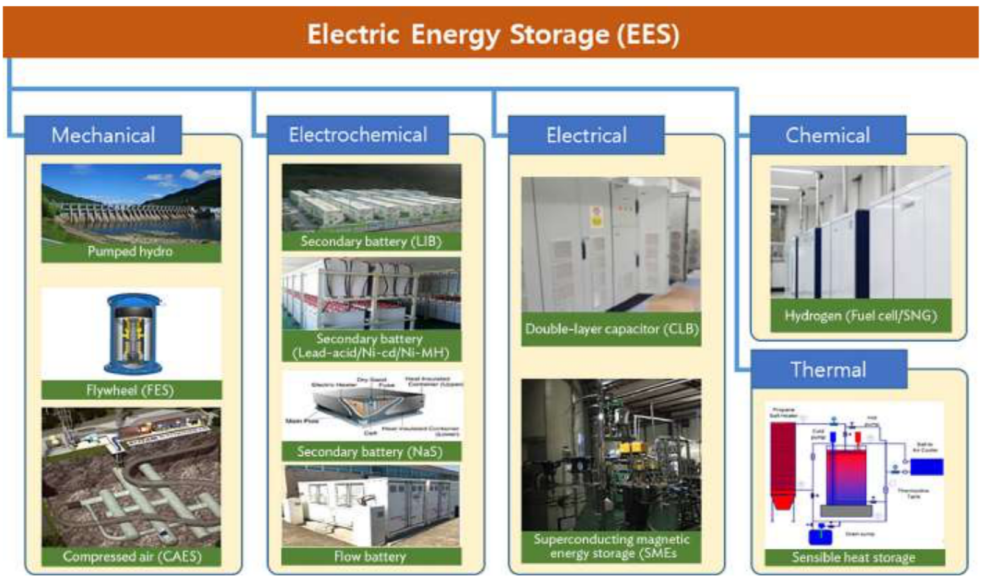

Figure 2.1: Classification of storage technologies, by energy type. [29]

1. Mechanical systems, such as compressed air energy storage (CAES), falling weights, pumped hydroelectric storage (PHS) and flywheel energy storage (FES);
2. Electrochemical systems, in particular different types of battery, among which are redox flow batteries;
3. Electrical systems, such as capacitors, supercapacitors, double-layer capacitors (CLBs) and superconducting magnetic energy storage (SMES);
4. Chemical systems, such as hydrogen storage with fuel cell/electrolyser, synthetic natural gas (SNG), and reversible chemical reactions;
5. Thermal energy storage (TES) systems, such as sensible heat storage, latent heat storage, as well as thermal absorption and adsorption systems.

Ideally, when developing energy storage technologies, certain properties should be taken into account: capacity reserve, quick response time, short or long-time storage, stationary or portable, conversion rate, energy density rating, storage costs, security, environmental impacts, end-use (e.g. grid connected or stand-alone), and storage time limits [28]. The main principle is that ESSs store energy during the times of low demand (if surplus energy is available), and deliver this energy during the times of high energy consumption, for example when energy production is not sufficient. Figure 2.2 shows how these technologies work [9].

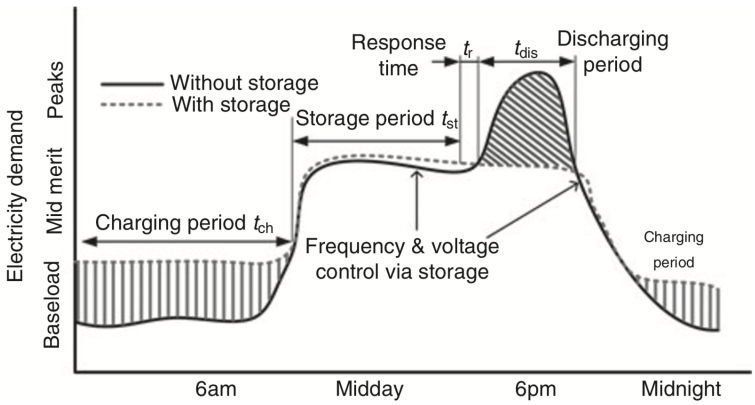

Figure 2.2: A simplified profile of charging and discharging for a typical ESS. [9]

As illustrated in Figure 2.2, the charging period (t_{ch}) for any ESS corresponds to late evening/night-time, when the energy is kept at baseload levels. However, as the day comes in, all the produced energy is destined to cover demand and the electrical loads increases. Depending on the size of the storage system utilized, discharging period (t_{dis})

accounts for the part of stored energy that is used to supplement energy production by covering parts of it or the entire energy deficit that appears as the electricity demand reaches peak levels (usually during the middle of the day and during the early evening). In this context, in order for scheduling to be accurate, the response time of energy storage (t_s) has to be taken into consideration. Anyway, as the energy demand gradually decreases and the storage unit is recharged because partly or entirely discharged during the previous time period, the daily cycle can be considered completed. Moreover, among the duties of ESSs there is also management of the power injections used to regulate frequency and voltage [9,30].

2.2 Redox flow battery technology

The first idea of a redox-flow battery dates back to 1970s, when the U.S. National Aeronautics and Space Administration (NASA) used Fe^{3+}/Fe^{2+} and Cr^{3+}/Cr^{2+} as redox couples on the positive and negative sides, respectively. Since then, the concept has been implemented and, as of today, all-vanadium redox-flow batteries, in which four oxidation states of vanadium are included – (V(V) and V(IV) on the positive side (Equation 1.1) and V(III) and V(II) on the negative one (Equation 1.2) – are in the spotlight in the RFBs research and development [31]. However, due to the corrosivity, hydrogen evolution, kinetics, materials cost and abundance of the metal ions in acidic solutions on which flow batteries are based on, large-scale commercialization of the former has been limited. Thus, research is focusing on developing and optimizing quinone-based flow batteries where the dangerous bromine, already in use instead of vanadium, can be replaced with the nontoxic ferricyanide ions [17]. The following sections describe the working mechanism and the caracteristics of a general redox-flow battery. Afterwards, alkaline quinone flow-batteries will be presented.

2.2.1 Working mechanism

Redox-flow batteries (RFBs) allow for energy conversions through reversible electrochemical reactions of two soluble redox couples. This type of battery is made of two parts connected to each other through pumps: the battery cell stack (where the reactions take place) and the external tanks, used to store the aqueous electrolytes [31]. The reactions happen during charge and discharge processes in the negative and positive compartment. During reduction, electrons and ions are extracted from one electrolyte;

later, these are recombined in the other electrolyte through oxidation [28, 32]:

Anode:

$$\begin{aligned} A^{n+} + xe^- &\rightarrow A^{(n-x)+}(charge, reduction) \\ A^{(n-x)+} - xe^- &\rightarrow A^{n+}(discharge, oxidation) \end{aligned} \tag{2.1}$$

Cathode:

$$\begin{aligned} B^{m+} - ye^- &\rightarrow B^{(m+y)+}(charge, oxidation) \\ B^{(m+y)+} + ye^- &\rightarrow B^{m+}(discharge, reduction) \end{aligned} \tag{2.2}$$

Figure 2.3 is a schematic illustration of a redox flow battery [32].

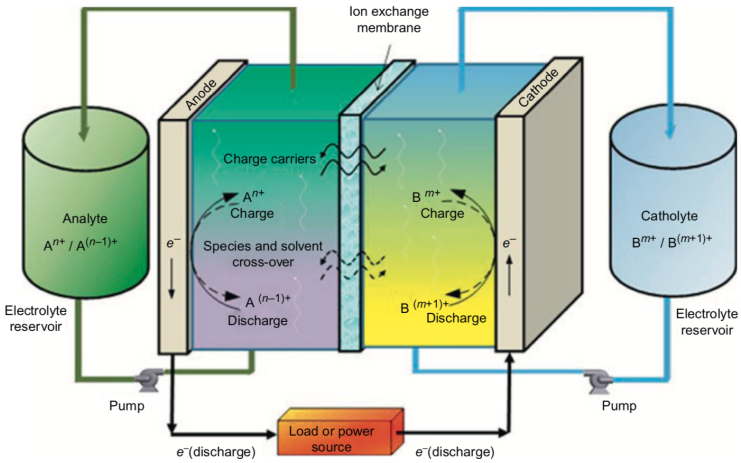

Figure 2.3: Scheme of a redox flow battery. [32]

As illustrated Figure 2.3, a membrane is placed between the electrodes with the aim of allowing the transport of charged ions (for example, H^+) and solvent in order to maintain electro-neutrality and electrolyte balance [31]. Moreover, the membrane serves to prevent electrolytes from crossing the membrane itself and mixing, in a process called 'cross-contamination', as this could lead to self-discharge, or degradation, of a battery [32]. Unlike conventional batteries, where the redox-active materials are stored inside the electrodes, redox flow batteries store energy in the electrolytes that are then pumped into the cell for energy conversion [28].

The main characteristic of redox flow batteries is their ability to separate power and energy, so that they are independent from one another: power rating is controlled in the cell stack by the operation current density and total electrode areas whilst energy, being stored in the external tanks, depends on the concentration of the active species,

the number of transferred electrons per mole of active redox ions during discharge, and the solution volume in the tanks [31–33]. For this reason, it is possible to obtain higher battery energy capacity only by increasing the volume of the electrolyte or the concentration of the active species [32]. Moreover, because of their flexible design that render them valuable and able to meet the demands of diverse energy-power ratios in the grid-scale energy storage industry [31, 32], redox flow batteries present many advantages:

1. **Long lifetime.** Depending on the type of active species employed, RFBs are expected to have a 10 years long lifetime because the active species are dissolved in the electrolytes and no phase change occurs in the electrodes.

2. **High energy efficiency.** It is possible for RFBs that the energy efficiency reaches up to 90 % under favorable low current density conditions. Moreover, after charging, anolyte and catholyte are stored in two different reservoir tanks; self-discharge rate, on the other hand, is rather low even after a long-term operation.

3. **Moderate cost, compared to lithium-ion batteries.** In order to reduce installation and maintenance cost, inexpensive materials are used for RFBs, such as carbon and plastic. Moreover, the cost for installation per unit of energy storage capacity ($/kWh) is also significantly reduced as energy storage system capacity increases.

4. **High charge rate.** It is possible to quickly and fully recharge the battery by simply replacing the electrolyte.

5. **Flexible operation.** Charging and discharging of RFBs can happen over a wide range of current. This represents an advantage of RFBs over conventional lead-acid batteries, as they can be deeply discharged without damaging the cell during charge and discharge cycles.

However, redox flow batteries show also disadvantages [29]:

1. **Complexity.** These systems require pumps, sensors, flow and power management, and secondary containment vessels.

2. **Low energy density.** Compared to other types of batteries, RFBs show lower energy densities.

Table 2.1 illustrates different batteries and their characteristics. It is possible to ascertain the cost-effectiveness of the RFB [32].

Table 2.1: Characterisctics of different batteries for energy storage. [32]

Type of battery	**Cycle life**	**Energy efficiency [%]**	**Installation cost [$/kWh]**	**Environm. influences**	**Deep discharge**	**Installation and maintenance cost [$/kWh]**
Lead acid	500	45	550	Moderate	Bad	3860
Nickel cadmium	800	70	1700	Moderate	Bad	2833
Zinc bromine	2500	68	520	Serious	Good	3191
Sodium sulfur	3000	80-85	1000	Moderate	Good	4639
Lithium ion	2000	90-95	3000	Slight	Bad	6346
All vanadium RFB	13000	75-85	989	Slight	Good	1327

2.3 Cell design

The components of a flow battery cell are a separator, usually an ion exchange membrane; two or more electrode layers on either side of the separator; a copper current collector; an insulator and a non-conductive plastic Teflon frame (the gasket) for each cell that delivers reactants to each electrode. These 'repeat parts' are assembled in layers to form a RFB stack and, then, those layers are integrated into a cell stack with two end plates and bolts that deliver the necessary mechanical compression [10]. Some of these components are shown in Figure 2.4 [34].

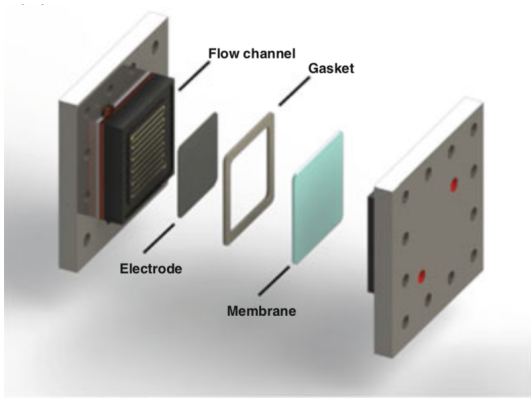

Figure 2.4: Exploded view of a redox - flow battery components. [34]

An ideal cell is able to minimize kinetic, ohmic and mass transport voltage losses. For this reason, improving of the cell design to achieve better battery performance usually aims at choosing electrodes that provide sufficient kinetic activity and membranes that allow a minimal crossover of the redox active species while exhibiting acceptable conductivity [35]. Hence, the hydrodynamics of a flow battery depends on the electrode morphology and on the flow field pattern jointly with the flow rate [36].

2.3.1 Electrolytes

An RFB electrolyte is typically composed of three species: a solvent, a supporting electrolyte, and the active species (the redox couple) [10]. Electrolytes are the most important components of a RFB, as the system - specific energy density depends on their concentration; thus, it is desired to use redox active agents with high solubilities [12]. Moreover, the temperature stability of the solution is also of great importance, as it defines the temperature window for the battery operations [31]: it is important for the electrolytes to be especially stable at $\sim 0\,\%$ and at $\sim 100\,\%$ SOC (state of charge) of the battery, when cell operation and electrolyte storage are severely tested [12]. Using aqueous electrolytes for redox-flow batteries, however, limits the electrochemical window of the battery (ca. 1.2 - 1.6 V) as water electrolysis happens beyond that threshold [37].

2.3.2 Electrodes

The electrode material has great importance in determining the optimal performances of a redox flow battery, as these can be achieved by managing electrochemical reactions and

electron/ions/species transport through the electrodes [38]. In fact, the electrochemical activity influences the overpotential loss and, thus, affects the voltage efficiency. Moreover, during charging and discharging of the battery, when the electrical current is passing through the electrode, the resistance of the electrode will influence the ohmic losses and these, in turn, will affect cell voltage and energy efficiency [39]. Thus, the electrodes should satisfy the following requirements [40]:

- High mechanical strength
- Be low cost and have a long lifetime
- Allowing fast electrochemical kinetics so that the overpotential can be decreased and high current densities can be achieved during charge/discharge cycles
- Exhibiting high porosity and specific surface area; in this way, high reaction area and ease of access to the internal surface enable high current densities

There exist three main types of electrodes for redox-flow batteries: carbon cloth, carbon felt and carbon paper electrodes. Carbon is widely employed because of its large operating potential range and its low cost [41].

- **Carbon cloth electrodes** present a high rate of mechanical degradation during the charging process, most likely due to the low surface area of the material itself and to the flow-by configuration [39,42].
- **Carbon felt electrodes** are the most utilized as they exhibit large specific surface area and high electrical conductivity. They show a three - dimensional network structure and, consequently, membrane punctures and short circuits are likely to happen [43]. Their low hydrophilicity has been enhanced with heat treatment, which made it possible to increase the concentration of oxygen functional groups on the felt surface [42]. Generally, carbon felt materials have a porosity of 0.8, a fibre diameter of approximately 10 mm and a permeability of 20×10^{8} cm^2 [44].
- **Carbon paper electrodes** show high porosity, low density and low electrical resistance. Moreover, it has been shown that thermal treatment of this material results in improved performance of the battery [44]. Moreover, carbon papers electrodes allow for a reduction in ohmic resistance of the cell, as the contact resistance within the cell is decreased [43].

The electrodes are shown in Figure 2.5.

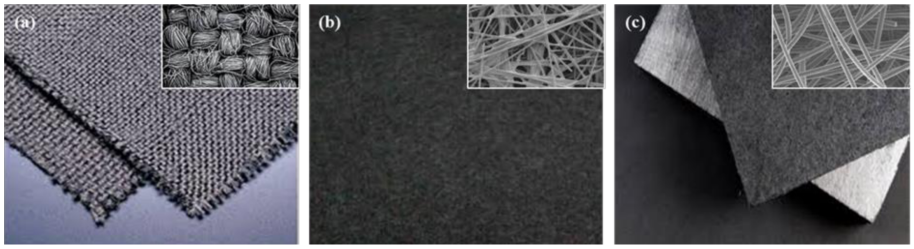

Figure 2.5: Comparison of electrodes for redox flow batteries: (a) carbon cloth electrode, (b) carbon paper electrode, (c) carbon felt electrode. [42]

2.3.3 Membrane

An ideal membrane for redox-flow batteries should be able to keep the anolythe and catholyte from mixing and, in the meantime, allowing the transport of the charge carrying ions to preserve the electric neutrality and electrolyte balance [45]. For RFBs, Nafion membranes are the most used [14]. Nafion is a hydrophobic and hydrophilic two-phase structure where the tetrafluoroethylene represents the backbone, whilst the sulphonate groups, terminated by pendant vinyl ether side chains, show hydrophilic property with proton conductivity [46].

2.3.4 Bipolar plates and flow fields

Bipolar plates, also called flow field plates, are necessary to deliver reactants to and remove products from the ion exchange membrane [47]. Therefore, whilst the flow-field design of the bipolar plates has the main task of achieving the maximum possible homogeneity over the cell's active area [48], the plates are built in order to connect cells electrically in series, provide structural support for the stack and house the flow field channels [47].

Bipolar plates are most commonly made of graphite because, despite its high cost, this material is very resistant to corrosion, it is chemically inert and shows good conductivity. However, since flow channels have to be either machined or electrochemically etched on the graphite plate surface, mass production of these cannot be achieved. Hence, thin layers metallic plates are replacing the graphite ones on the market [47].

There exist two different types of flow patterns for RFB: flow-through and flow-by design [49]. In the flow-through design, the bipolar plate do not present any channel and all the flow is forced through the electrodes, rendering the mass transport of reactants

within the electrodes excellent. However, ohmic losses are significant especially in large size cells, as the electrodes need to be very thick to minimize pressure drop [10]. In the flow-by configuration, instead, the flow field is designed on the bipolar plate, located adjacent to the porous electrodes resulting in a parallel flow field: the channels on the surface of the plate are open at both ends, ensuring flowing of the fluid through a continuous path from start to end, enabling reduction of pressure drops and delivering a fluid whose direction is perpendicular to the current. [49]. Moreover, flow-by configurations enhance localized mass transfer when coupled with carbon paper electrodes, because of their thinner thickness and their larger surface area-to-volume ratio [50]. Figure 2.6 illustrates the electrolyte flow for bipolar plates with 'flow-through' and 'flow-by' design [51].

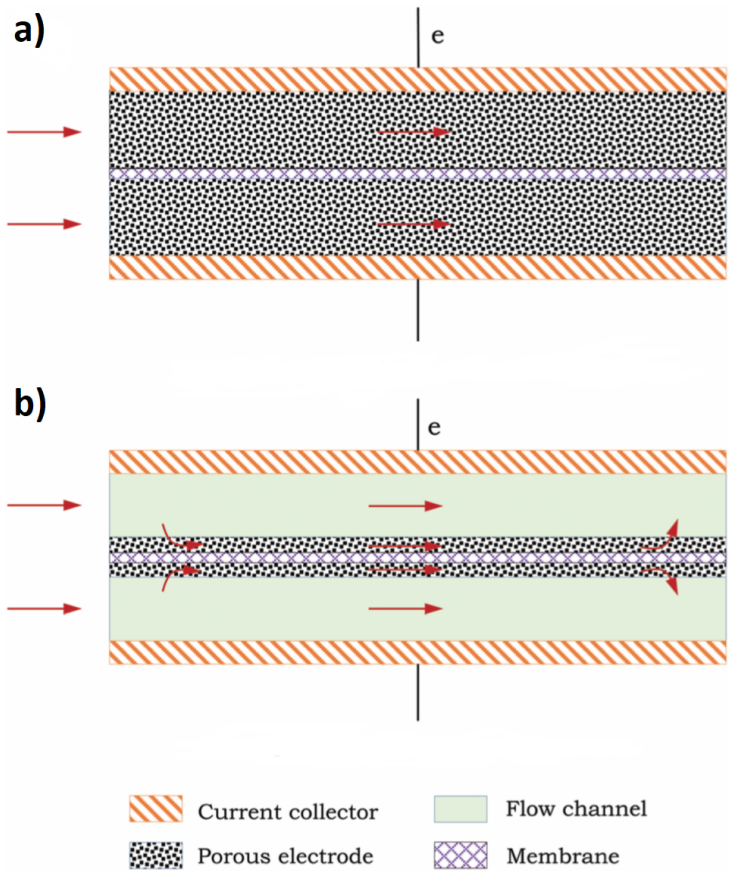

Figure 2.6: Two-dimensional configuration of (a) 'flow-through' design and (b) 'flow-by' design for bipolar plates [51]

Currently, the 'flow-by' design is used for bipolar plates that present serpentine flow field (SFF), as in Figure 2.7b [51].

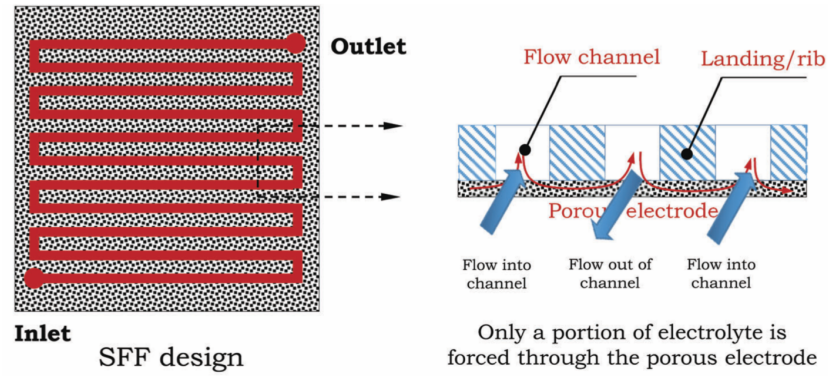

(a) Serpentine flow field (SFF) [51]

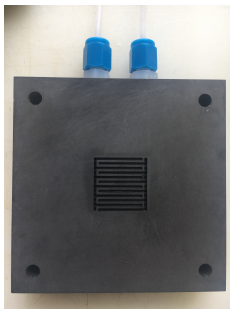

(b) Bipolar plate with serpentine flow field.

Figure 2.7

2.4 Quinone - based redox flow batteries

The most common all-vanadium redox flow batteries employ vanadyl sulphate in a sulphuric acid solution as initial electrolyte at both sides [32]. However, the high cost and low abundance of the metal ions have driven the attention on aqueous organic redox flow batteries (AORFBs), whose water-soluble organic redox-active molecules are made of earth-abundant elements, such as quinones, a class of natural and synthetic electron carriers compounds [18, 52]. Batteries using such molecules could run at acidic, neutral or basic pH [53]. For this reason, vanadium ions were initially replaced with bromine and anthraquinone ions [54], as the use of quinones in an acidic aqueous flow battery can significantly reduce the battery cost [17].

2.4.1 Quinones

Quinones belong to the class of quinoids, compound that are widely distributed in nature, for example in chlorophylle during photosynthesis [52]. They are aromatic compounds that, in aqueous environments, can be arranged in either para- $(p-)$ or ortho- $(o-)$ forms: the substituted dione is conjugated (it maintains the $-[C-H]=$ or $-[C=O]-$ single-double bond arrangements) to an aromatic nucleus (benzoquinones) or to a condensed polycyclic aromatic system (naphtoquinones and anthraquinones) [52, 55].

Quinones show two different electrochemical behaviors when reacting in aqueous or non aqueous media [56]. In non aqueous media, reduction of the quinones is represented by two successive one-electron reduction steps; the first one is completely reversible,

whilst the second one is quasi-reversible. A semiquinone radical ($Q^{\bullet -}$) is the result of the first step and a quinone dianon (Q^{2-}) is the result of the second one: the quinone radicals are short lived, therefore, the molecule undergoes disproportionation generating a quinone and its corresponding dianon. In aqueous media, instead, the general reduction mechanism for a para-benzoquinone is reported in Figure 2.8, where all the redox states presented are likely to happen [57]:

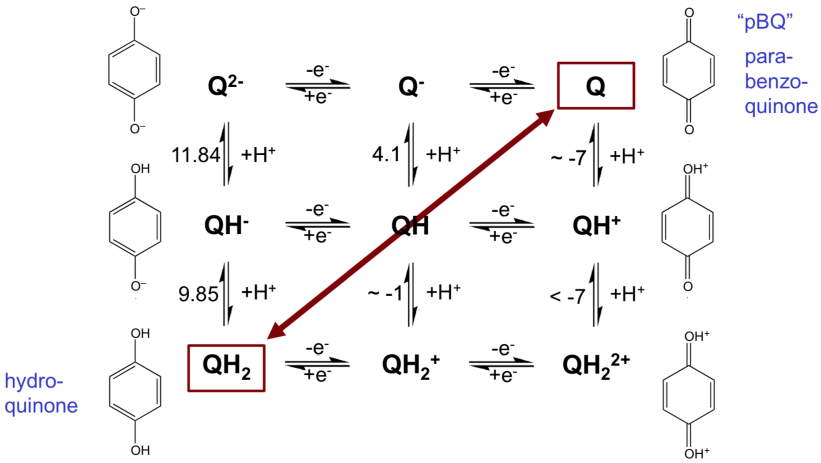

Figure 2.8: Proton and electron addition reactions with known and estimated pKa's for a general para-benzoquinone. [57]

The reaction is generally described as two rounds of electron-transfer coupled with proton acceptance, as shown in Equation 2.3.

$$\begin{aligned} Q + e &\rightleftharpoons Q^{\bullet -} \\ Q^{\bullet -} + H^+ &\rightleftharpoons QH^{\bullet} \\ QH^{\bullet} + e &\rightleftharpoons QH^- \\ QH^- + H^+ &\rightleftharpoons QH_2 \end{aligned} \tag{2.3}$$

At acidic pH, the reduction reaction proceeds rapidly with two protons and two electrons, as in Figure 2.9.

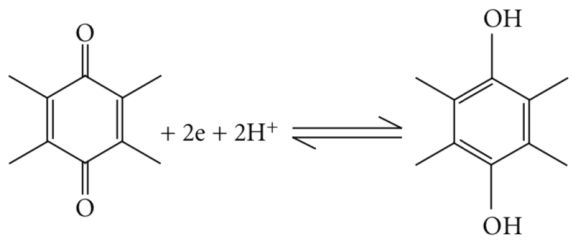

Figure 2.9: Two-electron two-proton reduction of quinone in acidic aqueous media. [56]

The quinone on the right side of Figure 2.9 is called *hydroquinone*, a benzene ring with hydrogens on all the corner except for two hydroxy- groups. Pulling off two electrons and two protons from the hydroquinone results in the compound shown on the left side, which is called *benzoquinone* and is the simplest quinone [58].

In alkaline aqueous media, on the other hand, the reaction takes place without the presence of protons, as shown in Figure 2.10, and the quinone is reduced to its dianon (Q^{2-}) [56].

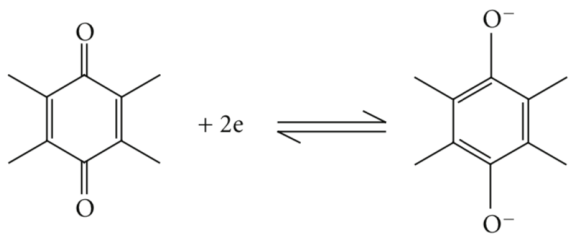

Figure 2.10: Two-electron reduction of quinone in alkaline aqueous media. [56]

At neutral pH, instead, the reduction reaction is either by one proton two electrons or only two electrons without the participation of protons.
Anyway, the electron transfer reactions involving quinones are reversible and this is due to the resonance-stabilization of semiquinone radical intermediates, which arises, in turn, from the delocalization of electrons over a given molecular structure [55]. For example, a para - semiquinone radical is extremely stable because the hydroxy substituents are placed in para - positions of the phenoxy radical for p - resonance interactions. Hence, para-semiquinone anions show over 60 % of electron density on the hydroxy oxygen, resulting in the reversible redox chemistry [59].

Figure 2.11 is an example of the redox mechanism that quinones undergo during photosynthesis, where the quinone accepts electrons from the clorophylle [58].

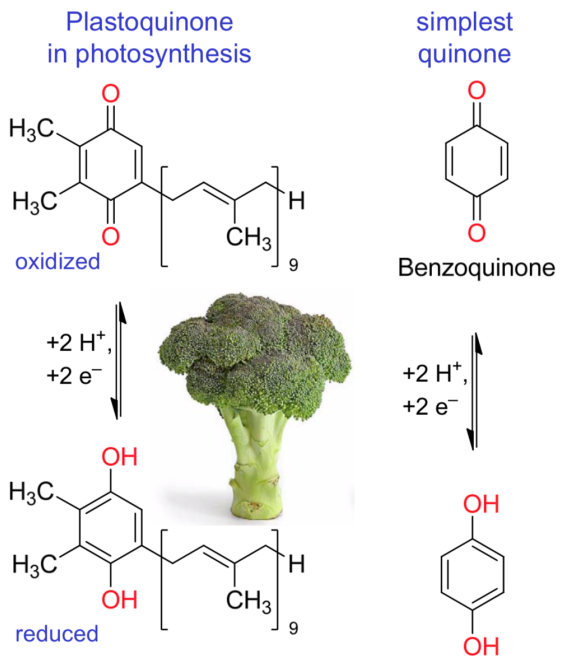

Figure 2.11: Example of benzoquinone undergoing reversible reduction and oxidation during photosynthesis. [58]

However, more complicated two- and three- benzene rings quinones exist, as shown in Figure 2.12 [55, 58].

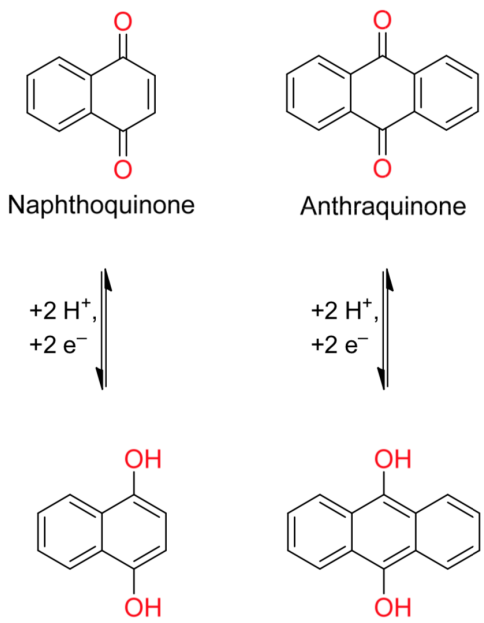

Figure 2.12: Reduction and oxidation processes for naphtoquinone (left) and anthraquinone (right). For both the compounds: on the bottom is the reduced form, on the top is the oxidized form. [58]

2.5 Evaluation characteristics

As flow batteries are considered secondary batteries (rechargeable batteries), their electrochemical properties and performance can be evaluated through different parameters [32, 60]:

1. **Coulombic efficiency, η_C :** it represents the reversibility of the electrochemical reactions occurring within the system and it is used to predict the battery life.

$$\eta_C = \frac{I_D\, t_D}{I_C\, t_C} \times 100\,\% \tag{2.4}$$

   where I_D and I_C are the discharging and charging cell currents, respectively, and t_D and t_C discharging and charging time, respectively. The ideal efficiency of a battery is represented by the unity; therefore, the more undesired reactions take place in the stack, the more the efficiency will deviate from unity and the shorter the life of a battery will be.

2. **Voltage efficiency, η_V :** it is the ratio of cell voltage during discharge to cell voltage during charge.

$$\eta_V = \frac{V_D}{V_C} \times 100\,\% \tag{2.5}$$

3. **Produced electrical energy.** It is known that flow batteries store energy in a chemical form to release it as electrical energy when needed, therefore, calculating the electrical energy produced is important when comparing the behavior of different storage systems. As power is calculated as follows:

$$P = I \times V \tag{2.6}$$

   where I is the electric current in amperes and V is the electric potential or voltage; the produced electrical energy is:

$$E = \int_0^t P\, dt \tag{2.7}$$

4. **Energy density.** This parameter measures the ability of a system to store energy in a given volume. For high energy density systems, it is possible to store a high amount of energy in a small volume.

$$ED = \frac{n\,C\,F\,V}{\mu_v} \tag{2.8}$$

where n is the number of electrons transferred during the reaction, C is the lower concentration of the two electrolytes, F is the Faraday's constant (96.485,33289 C/mol), V is the open-circuit voltage of the battery, and μ_v is the volume factor (μ_v = 1 + lower electrolyte concentration/higher electrolyte concentration). The energy density is calculated based on the discharging process [32].

5. **Current density [$\vec{J}$].** It represents the amount of charge per unit time that flows in a unit area of a chosen cross section. Current density is strictly related to the flow field design of a battery, as the maximum current density corresponds to 100 % utilization of the redox active species that penetrate into the porous electrodes when the electrolytes flow through the flow field [61]. In this regard, it is possible to define the limiting current density as in Equation 2.9 [62]:

$$\vec{J}_{lim} = \frac{a\,t_p\,n\,F\,D\,c}{\delta_b} \tag{2.9}$$

where a is is the interfacial porous electrode surface area per unit porous electrode volume, t_p is the thickness of porous electrode, n is the number of electrons transferred per mole of species reacted, F is the Faraday constant, D is the diffusivity, c is the bulk electrolyte concentration and δ_b is the thickness of diffusion boundary layer. The current flowing through the cell, in fact, depends on the diffusion boundary layer near the electrode-electrolyte interface [62].

6. **Energy efficiency [η_E].** It is the ratio of energy during the discharge process to energy during the charge process:

$$\eta_E = \frac{V_D\,I_D}{V_C\,I_C} \times 100\,\% = \frac{energy\,density_{\,discharge}}{energy\,density_{\,charge}} \times 100 \tag{2.10}$$

where V_D and V_C are the average discharge and charge voltage during the operations of the cell.

7. **Power density.** It represents the amount of power per unit area of a system. A high power density battery can deliver a high amount of energy to a relative small system:

$$PD = \frac{I \times V}{S} \tag{2.11}$$

where S is the surface area of the membrane or electrode geometric area.

8. **Capacity.** This parameter is measured in ampere-hours (Amh) or watt-hours (Wh) and describes the amount of energy that can be stored in a system. For example, a capacity of 1 Ah means that the battery will deliver one ampere of current in one hour. Therefore, the capacity of a battery corresponds to the amount of electric charge that is accumulated during the charging period, stored during the open circuit stay and, then, delivered during the discharge period in a reversible way [63]. It is possible to distinguish a theoretical capacity and a practical one for every battery.

   - **Theoretical capacity** is connected to the Faraday constant $F = 96485\, C/mol$. In order to calculate the total amount of electrons that are transferred from one half-cell to the other during a reaction, it is necessary to use the following formula:

     $$Q_{th} = F \times n_{e^{-1}} \times c_{Quinone} \times V_{solution} \tag{2.12}$$

     where $n_{e^{-1}}$ is the number of electrons lost per quinone molecule, $c_{Quinone}$ is the concentration of the quinone and $V_{Solution}$ is the volume of the solution.

   - **Practical capacity** can be measured when the cell is fully discharged; hence, it is necessary to start with a fully charged cell and then draw a constant current of X amperes until the cell is fully discharged. A cell is considered fully discharged when its voltage reaches the end of discharge voltage $(EODV)$. The discharging will take a certain amount of time (T) [64]. Therefore, the capacity is equal to

     $$Q_p = X \times T \tag{2.13}$$

     when the current vs. time curve is not a curve, but a straight line. Otherwise, if the current vs. time curve is indeed a curve, it is necessary to calculate it as the area under the discharge curve.

It is to be mentioned that practical capacity will always be smaller than theoretical capacity as not all the molecules present in the electrolytes will undergo redox reactions; thus, the remaining molecules will not give their electrons up and, therefore, there will not be a decrease in capacity.

2.6 Electrochemical cell and reactions

Redox flow batteries are electrochemical cells belonging to the category of galvanic cells, characterized by reactions occurring spontaneously at the electrodes when connected externally by a conductor, and that are employed for conversion of chemical energy into electrical energy. For these cells, it is possible to measure the difference in electric potential between two electrodes, in order to get the amount of energy available to drive charge externally between electrodes [65].

The electrical energy obtained from chemical reactions is able to produce work (w_{ele}). This work is the product of the potential difference (voltage) multiplied by the charge transferred (Q), as in Equation 2.14 [66]:

$$w_{ele} = volts \times Q \tag{2.14}$$

Q represents the charge in Coulombs (C), or the number of electrons that cross an interface when a change in the system happens due to variation in the potential E_{cell} of the cell, which causes a current flow in the external circuit. The relationship between charge and amount of product is given by *Faraday's law*: the passage of 964845.4 C (*Faraday's constant*) causes consumption of 1 mole of reactant or production of 1 mole of product in a one-electron reaction [65]. Therefore:

$$total\,charge = (number\,of\,moles\,of\,e^{-}) \times F = n\,F \tag{2.15}$$

The maximum potential E_{cell} that a cell can produce is related to the electrical work (w_{ele}) as in Equation 2.16 [66]:

$$E_{cell} = \frac{-\,w_{ele}}{n\,F} \tag{2.16}$$

where the negative sign for w_{ele} represents a work that is done by the system (the galvanic cell) on the surroundings [66]. Remembering that $\Delta G = w_{max} = w_{ele}$ [65], the free energy (ΔG) is related to the charge passed and the (reversible) potential difference, as in Equation 2.17:

$$\Delta G = -\,n\,F\,E_{cell} \tag{2.17}$$

Equation 2.17 can be rewritten as follows:

$$\Delta G^\circ = -\,n\,F\,E^\circ{}_{cell} \tag{2.18}$$

when all the reactants and products are in their standard states [66].
Since $\Delta G^\circ = -\,R\,T\,\ln K$, the standard cell potentials can be related to the equilibrium constants in the following way [65]:

$$E^\circ{}_{cell} = \frac{R\,T}{n\,F}\,\ln K \tag{2.19}$$

According to Equation 2.19, it is possible to relate non-standard conditions redox equations to free energy and cell potentials. Considering a general cell, the free energy can be written as [66]:

$$\Delta G = \Delta G^\circ + R\,T\,\ln Q \tag{2.20}$$

where Q is the reaction quotient. Since $\Delta G = -\,n\,F\,E_{cell}$ and $\Delta G^\circ = -\,n\,F\,E^\circ{}_{cell}$, the potential of a cell is described by the following equation, called *Nernst equation* [66]:

$$E_{cell} = E^\circ{}_{cell} - \frac{R\,T}{n\,F}\,\ln Q \tag{2.21}$$

If a system follows Equation 2.21, or any equation derived from it, the electrode reaction is often said to be thermodynamically or electrochemically reversible (or *nernstian*) [65].

3. Experimental considerations

3.1 Experimental considerations

This section gives a brief overview of the experimental plan designed for this thesis and Table 3.1 is an overview of the main investigations carried out.

Table 3.1: Brief overview of the main investigations carried out.

Experiment	Method	**Motivation**
I	Cyclic voltammetry	To monitor electrochemical behavior of the species to be employed as electrolytes in the battery, to obtain information about their reduction potentials and to investigate reversibility of redox reactions.
II	Cell cycling tests	To evaluate the performance of the flow battery operated with the previously chosen chemicals.
III	Limiting-current technique	To determine the maximum reaction rates and mass-transfer coefficients.

3.1.1 Experiment I

According to *Uchimiya M. and A. T. Stone* [55], the electron transfer reactions involving quinones are reversible; therefore, such species can be employed as electrolytes for redox flow batteries. One way of confirming the reversibility of the redox reactions and

determine cell potential values is represented by cyclic voltammetric experiments, as reported by extensive literature [11, 67]. As recent literature data (*Lin et al. (2015)* [17] and *Yang et al. (2017)* [18]) have used cyclic voltammetric investigations to prove the success of the redox couples 2,6-DHAQ/ferricyanide and 2,5-DH-1,4-BQ/ferrocyanide as substitutes of the vanadium redox couple for flow batteries, the main idea of this part of experiments was to test multiple quinones, in order to find the ones whose performance could be compared to or exceed the above mentioned quinones.

3.1.2 Experiment II

As these experimental investigations represented an uncharted territory, the best available option was to try to reproduce the same results as *Lin et al. (2015)* [17] and *Yang et al. (2017)*, who have been among the first to experiment the performance of quinone-based flow batteries in alkaline solutions, as electron donating groups, such as (OH^-), could lower the reduction potentials and expand the battery voltage. Once acceptable results would have been obtained, the plan was to operate minor changes in the procedure in order to optimize the performance of the newly acquired flow cell.

3.1.3 Experiment III

It is generally known that, for a redox reaction happening on the surface of an electrode, there exist a driving force for transport of analyte to or from the electrode surface when the concentrations near the electrode surface are not the same as the corresponding concentrations in the bulk of solution [68]. If electron transfer is fast (i.e., the electrode reaction is reversible), the current flowing is determined solely by the rate of mass transfer of analyte to the electrode surface [69]. Therefore, according to *Muff et al. (2012) [70]*, the limiting-current technique was believed to be a useful tool to get information about mass transfer coefficient and, in turn, about the limiting current density. It is to be noted that the above mentioned studies employed a one-compartment electrochemical cell, whilst the cell used in this project is characterized by the presence of an ion-exchange membrane between two flow plates.

4. Materials and Methods

This chapter discusses the main materials employed and the procedures used in testing the performance of the redox flow battery. According to *Lin et al. (2015)* [17] and *Yang et al. (2017)* [18], it is possible to adapt quinone-based flow batteries to alkaline solutions where the bromine is replaced with the nontoxic ferricyanide ion at the positive side of the battery and highly soluble hydroxylated anthraquinones and benzoquinones are employed as anolytes.

4.1 Materials

In this section, the main compounds and supporting electrolytes used throughout the experiments will be introduced and discussed.

4.1.1 Supporting electrolytes

Supporting electrolyte salts provide conductivity to the solution but, being electrochemically inert, do not participate in the electrochemical reactions. Demineralised water is used as the solvent.

4.1.1.1 Sodium hydroxyde

Sodium hydroxyde (NaOH) was used as the main supporting electrolyte throughout the whole experimental part, chosen because of its highly caustic basic and alkali properties. It has been used in two concentrations: 1 mol/L and 2 mol/L. When used in the lower concentration, it was used as purchased, in form of a liquid; in the higher concentrations, NaOH in form of a white hygroscopic crystals was dissolved in deionized water.

4.1.1.2 Sodium sulfate

Sodium sulfate was used as the supporting electrolyte for the redox couple ferro/ferricyanide during mass transport coefficient investigations. It is an electrolyte salt that allows the passage of current through the solution and prevents charge buildup at the electrodes. In the purchased form, sodium sulfate is a white hygroscopic crystalline powder that was dissolved in deionized water and used in three different concentrations: 1 mol/L, 0.1 mol/L and 0.001 mol/L.

4.1.2 Electrolytes

For all the investigations carried out throughout the thesis, the compounds used were potassium ferricyanide ($K_3Fe(CN)_6$), potassium ferrocyanide ($K_4Fe(CN)_6 \cdot 3H_2O$) and petro-quinones. All the quinones available in the laboratories of the section of Chemical Engineering of Aalborg University Esbjerg were purchased from Sigma Aldrich and used as received, in form of a powder. According to their different chemical structures, quinone compounds can be divided into benzene quinones (one ring), naphthalene quinones (two rings) and anthraquinones (three rings). Table 4.1 shows the quinones used for cyclic voltammetry investigations and their respective concentrations.

Table 4.1: Analyzed quinones.

Quinone	Molecule	Concentration [mM]	Solvent
2,6-DHAQ	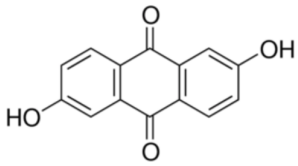	10	1 M NaOH
1,8-DHAQ	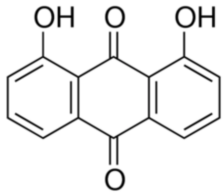	2	1 M NaOH
1,5-DHAQ	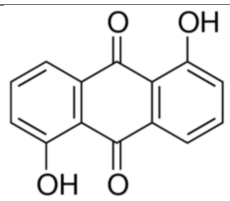	10	1 M NaOH
1-HA-9,10-Q	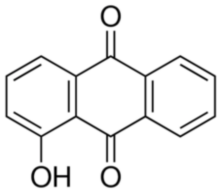	10	1 M NaOH
1,4-NQ	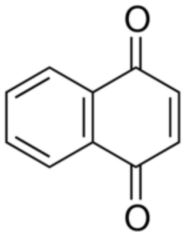	10	1 M NaOH
TF-1,4-BQ	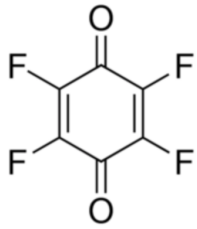	10	1 M NaOH
2,5-DH-1,4-BQ	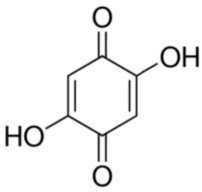	2	1 M NaOH

4.1.3 Cell components

The cell used for cycling experiments was acquired from the Department of Chemical Engineering of Aarhus University and provided from Fuel Cell Technologies (FCT). Figure 4.1 presents an exploded view of the cell configuration employed during this project.

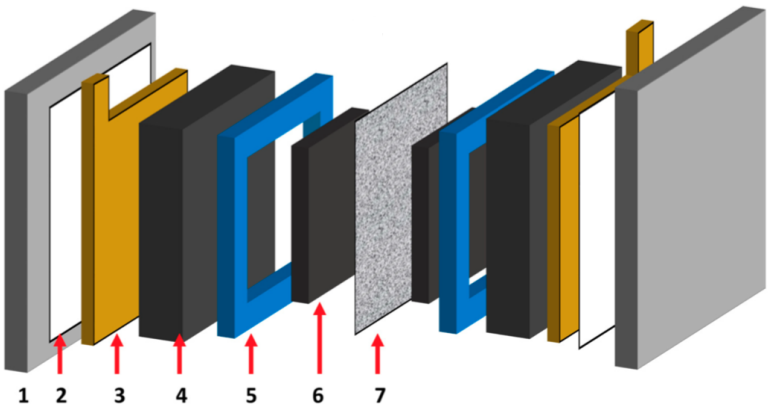

Figure 4.1: Components of the cell used for test and assembling order: (1) stainless steel endplate; (2) polytetrafluoroethylene sheet; (3) gold-plated copper current collector; (4) graphite block containing serpentine flow inlet and outlet (not shown); (5) teflon gasket; (6)carbon paper electrode; (7) Nafion®212 membrane.

Figure 4.2 illustrates each single component of the tested cell. The graphite bipolar plates (4) are engraved with a machined single serpentine flow channels that enables good removal of liquid electrolytes due to the high flow velocity and coverage of the entire active area, which measures 6.25 cm^2. The land in between the flow channels serves as current collection and transmission from one cell to another and to transfer the heat generated around the membrane area because of the chemical reactions [47]. Membrane, electrodes (6), Teflon gaskets (0.5 mm) (5) and current collectors (3) are in direct contact to achieve a 'zero-gap' configuration: ionic and contact resistance between the membrane and the electrodes are minimized. A sheet of untreated Nafion®212 membrane served as a separator and as the ion-selective membrane. Polytetrafluoroethylene sheets (2) were used as insulators between the current collectors, adjacent to the graphite blocks, and the stainless steel endplates (1). The cell was compressed together using eight M6 bolts (7) positioned evenly around the squared endplates. Before cell cycling experiments, Sigracet ®GDL 34 BA ($\sim$ 280 μm thickness) porous ($\sim$ 83 %) carbon paper was pretreated by baking in air at 500° C for 7 hours. When tests were not run, the cell was always flushed, disassembled and the membrane was stored in demineralized water to avoid

drying out.

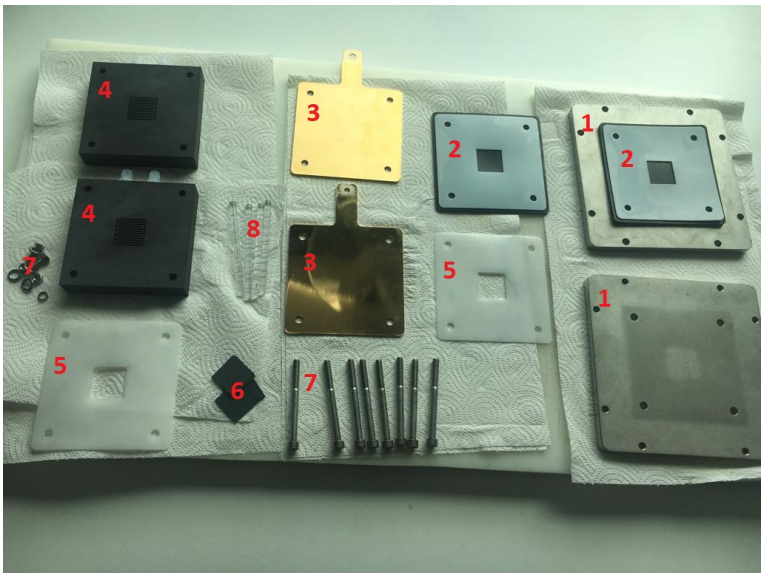

Figure 4.2: Disassembled view of the newly acquired redox flow cell: (1) stainless steel endplate; (2) polytetrafluoroethylene sheet; (3) gold-plated copper current collector; (4) graphite block containing serpentine flow inlet and outlet; (5) teflon gasket; (6) carbon paper electrode; (7) M6 bolts; (8) plastic aligners.

4.2 Methods

The present thesis exhibits the following structure: this section first presents the analytical method used to choose the most suitable chemicals to operate the battery with, then a description of the working configuration and setup of the cell cycling tests will be provided and, lastly, a brief description of the limiting-current technique will be introduced. The results of the experiments are discussed right after the description of each experiment itself.

4.2.1 Cyclic Voltammetry

Cyclic voltammetry is a widely used technique that allows for acquisition of qualitative information about electrochemical reactions. In this way, thermodynamics of redox processes, kinetics of heterogeneous electron-transfer reactions and reversibility of chemical reactions can be investigated. The method consists of scanning linearly the potential of the working electrode, immersed in a unstirred solution, using a triangular

potential waveform, as in Figure 4.3 where the reference electrode used is the saturated calomel electrode (SCE).

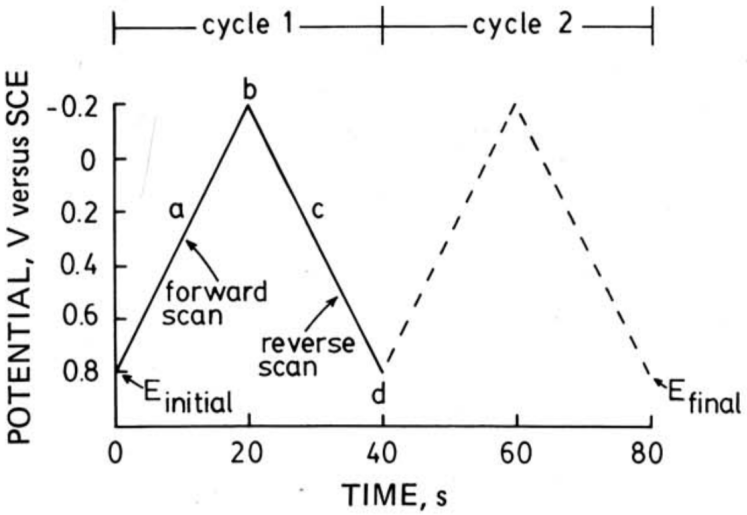

Figure 4.3: Potential-time excitation signal in cyclic voltammetric experiment [67].

During the potential sweep, the potentiostat measures the current resulting from the controlled potential applied between the working electrode and the reference electrode, whilst electrochemical reductions or oxidations reactions occur. The potential applied can be considered as an *excitation signal* that sweeps the potential between two values, called the *switching potentials*. In Figure 4.3, the excitation signal causes the potential to first start scanning negatively (forward scan, from +0.8 V to -0.2 V vs. SCE) and, then, at -0.2 V vs. SCE the scan direction is reversed, causing the positive scan back to +0.8 V vs. SCE (reverse scan). By measuring the current at the working electrode during the potential scan, a cyclic voltammogram is obtained, as in Figure 4.4. The peculiar shape of this voltammograms will be discussed along with the results of the investigations in chapter 5. Anyway, important parameters that can be obtained from cyclic voltammetry and that characterize the cyclic voltammogram of a reversible process are peak separation ($\Delta E_p = |E_{pc} - E_{pa}|$), peak current ($i_{pa}$ and i_{pc}) and peak ratio ($\frac{i_{pa}}{i_{pc}}$), as illustrated in Figure 4.4.

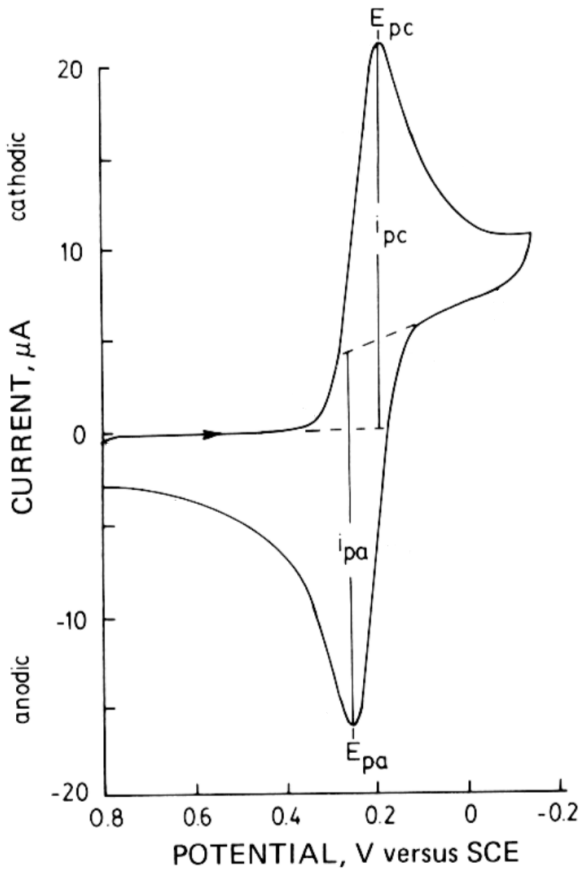

Figure 4.4: Typical curve for cyclic voltammetry (with SCE used as reference electrode) [67].

Through current peak ratio ($\frac{i_{pa}}{i_{pc}}$), it is possible to prove the reversibility of the electron transfer reactions and to directly observe the stability of the electrochemically generated product. When Equation 4.1 can be observed for a redox species being analyzed, the product is stable on the time scale of the experiment and the reaction being studied is reversible in both directions.

$$\frac{i_{pa}}{i_{pc}} = 1.0 \tag{4.1}$$

The values of peak current (i_{pa} and i_{pc}) are indicative of whether the analyte of an electrochemically reversible electron transfer processes is freely diffusing in solution or is absorbed on the electrode, through the Randles-Sevcik equation (Equation 4.2). The equation describes how the peak current i_p increases linearly with the square root of the scan rate v [$V\ s^{-1}$], where n is the number of electrons transferred in the redox event, A [cm^2] is the electrode surface area (usually treated as the geometric surface area), D_0 [$cm^2\ s^{-1}$] is the diffusion coefficient of the oxidized analyte, and $C°$ [$mol\ cm^{-3}$] is the

bulk concentration of the analyte [71]:

$$i_p = 0.446\, n\, F\, A\, C^{\circ}\, (\frac{n\, F\, v\, D_0}{R\, T})^{\frac{1}{2}} \tag{4.2}$$

Equation 4.2 expresses the relationship between the velocity of the scan rate and the size of the diffusion layer: the faster the scan rate, the smaller the diffusion layer, the higher the current observed on the duck-shaped plot [71]. However, investigations about the size of the diffusion layer were not carried out during this project.

Once the reversibility of the reaction has been proven from Equation 4.1, it is possible to calculate peak separation and obtain the number of electrons n transferred in the electrode reaction, as in Equation 4.3. When the reduction process is chemically and electrochemically reversible, the difference between the anodic and cathodic peak potentials (ΔE_p), is 57 mV at 25 °C (2.22 RT/F), and the full-width at half-max on the forward scan of the peak is 59 mV for one electron transfer fast reaction [71].

$$\Delta E_p = |E_{pc} - E_{pa}| = \frac{0.059\, V}{n} \tag{4.3}$$

Moreover, the values of E_{pc} and E_{pa} are necessary in order to calculate the formal potential[1] for a redox couple ($E^{\circ\prime}$) and, in turn, the theoretical potential of the cell when the formal reduction potentials are known for both species that form an electrolytic cell.

$$E^{\circ\prime} = \frac{E_{pa} + E_{pc}}{2} \tag{4.4}$$

4.2.1.1 Experimental procedure

Cyclic voltammetry (CV) investigations were conducted on a 2 µ AUTOLAB Type III potentiostat / galvanostat (Metrohm Autolab Instruments, Netherlands) using a three-electrode technique with Pt – RDE (rotating disc electrode, for cycling inorganic species; glassy carbon electrode, for cycling organic species) as the working electrode, Pt – wire as the counter electrode that conducts electricity from the signal source to the working electrode (non-reactive high surface area electrode, commonly platinum gauze) and a silver/silver chloride (Ag/AgCl) as reference electrode, which maintains a constant potential. Figure 4.5 illustrates the three-electrode configuration used during the experiments: the working electrode, connected to the red cable, is a glassy carbon

[1]The formal potential is the reduction potential that applies under a specified set of conditions.

electrode as the species in the cell is a quinone. The reference electrode is positioned close to the working electrode to minimize the IR (ohmic) losses between the two electrodes caused by the resistivity of the solution phase.

Figure 4.5: Cell for cyclic voltammetric experiments with three-electrode configuration. Red electrode is the working electrode, blue electrode the reference electrode and black electrode the counter electrode.

The potential of the Ag/AgCl reference electrode is +0.213 V vs. the standard hydrogen electrode (SHE). Cyclic voltammograms (CVs) were recorded of $K_3Fe(CN)_6$ and quinones dissolved in 1 M NaOH. When scanning the potential for the ferro/ferricyanide couple, a rotating disc electrode as Figure 4.6 was used as working electrode, which is able to promote electron flow so that diffusion layer is overcome when employed at faster rotation speeds. However, at 100 rpm (condition applied during these investigations), it is mainly used to achieve cleaner spectra.

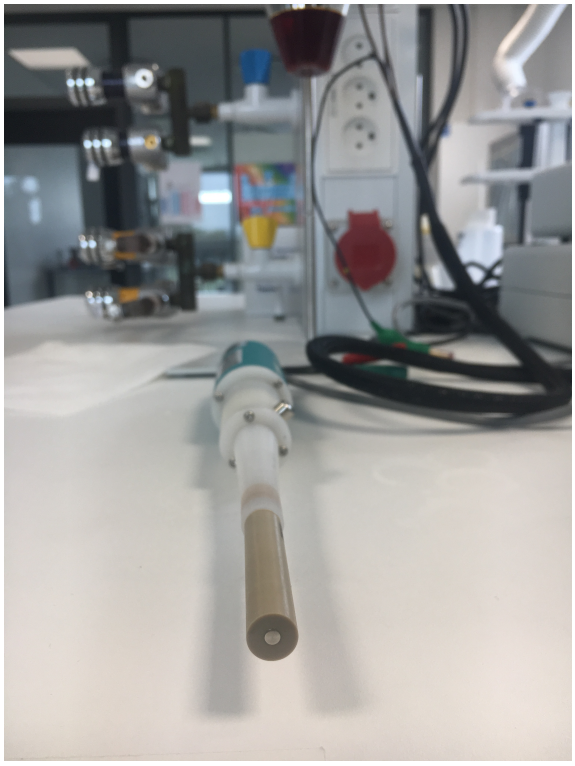

Figure 4.6: Pt-RDE.

The current flowing between the counter and working electrode was recorded and plotted as current (i) versus potential (E) through Nova 2.1 program, returning the so called 'duck-shaped' voltammograms.

Figure 4.7 presents the entire setup used for cyclic voltammetry technique: the three electrodes (to the left) are connected to the potentiostat (middle) which is, in turn, connected to the computer where the voltammograms are displayed (to the right). Through the tool on top of the potentiostat it is possible to control the spinning rate of the rotating disc electrode, which was kept at a constant rate of 100 rpm for all the experiments.

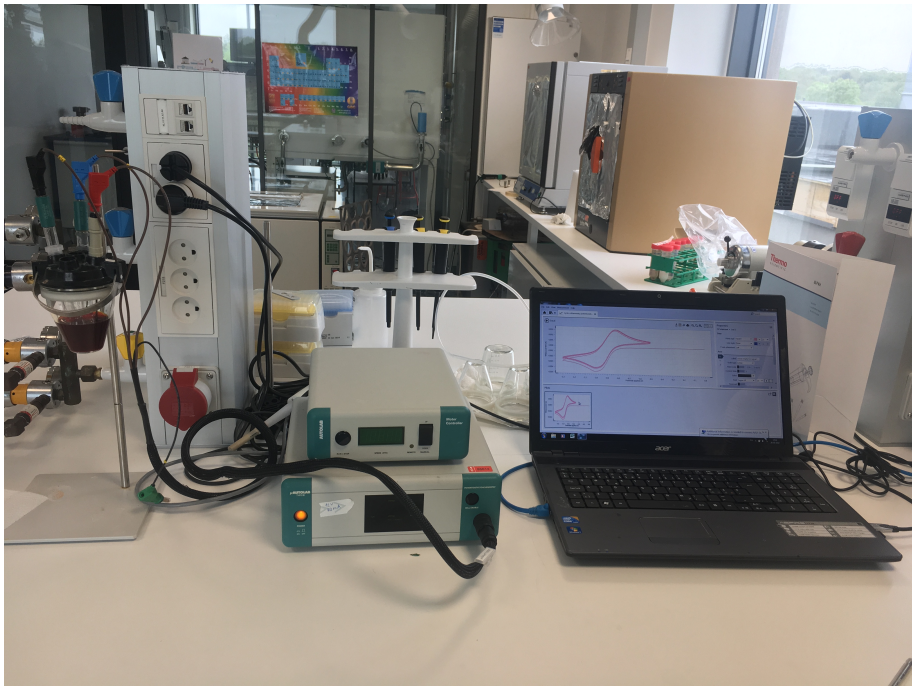

Figure 4.7: Cyclic voltammetry setup.

Alkaline solutions of each species reported in Table 4.1 were prepared as follows: according to the concentrations chosen, the quinones were weighted and dissolved in 50 mL of 1 mol/L NaOH, let on a stirring plate overnight and used the following day. Figure 4.8 shows the quinones solutions after overnight stirring.

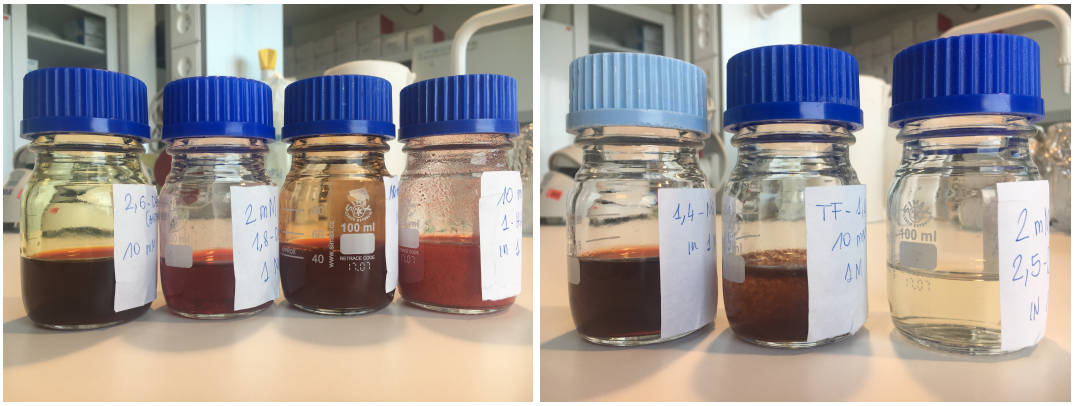

Figure 4.8: Quinones used for cyclic voltammetry investigations. From left to right, the order follows Table 4.1.

The catholyte used for cyclic voltammetry investigations was a volume of 50 mL of potassium ferricyanide 10 mM in 1 mol/L NaOH, prepared following the same procedure used for the anolytes.

Once the electrolytes were prepared, they were poured in the beaker, the beaker was sealed and the following initial conditions for cyclic voltammetry investigations were applied through Nova 2.1 program:

Table 4.2: Initial conditions for cyclic voltammetry investigations.

Starting potential (V)	0.000
Upper vertex potential (V)	2
Lower vertex potential (V)	-2
Stop potential (V)	0.000
Number of scans	4
Scan rate (V/s)	0.5

The potentiostat was started and the data were collected. Once the four scans were over, on the screen of the PC a voltammogram was visible. The voltammogram ranges between the values of upper (2 V) and lower (-2 V) potentials: therefore, it is possible to zoom in and search for the peaks that outline the duck-shaped diagram. Afterwards, the investigations on the same electrolyte were repeated by replacing the initial upper and lower vertex potential, in order to obtain a suitable duck-shaped diagram for interpreting the data. Throughout all the investigations, the scan rate of the cycled potential was always kept at the constant value reported in Table 4.2. The main tools used to interpret the results obtained are Equation 4.1, Equation 4.3 and Equation 4.4.

4.2.2 Cell cycling experimental procedure

As illustrated in Figure 4.9, cell cycling experiments were carried out connecting the newly acquired cell to the Neware battery tester (Figure 4.9a). A peristaltic pump (Shenchen LabV1, China) was used to flow the electrolytes through the cell (Figure 4.9b). The maximum achievable rate of the pump was 21.00 mL/min. Tubes with 13 mm diameter were used to transport the electrolytes between the feeder tanks and the cell.

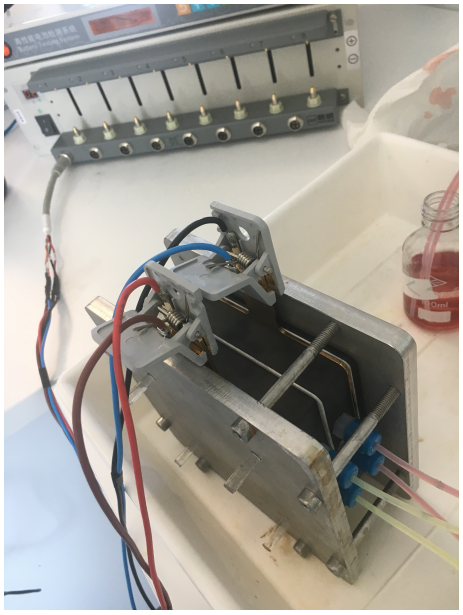

(a) Cell connected to the battery tester.

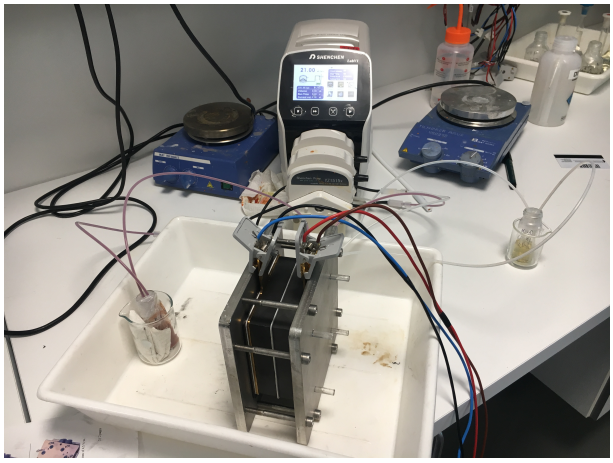

(b) Pump feeding the electrolytes to the cell.

Figure 4.9

Once the setup was ready and the electrolytes were fed into the cell, the battery tester was started. The conditions applied for cell cycling test are reported in Table 4.3. It was decided to always run 5 cycles for each electrolytic couple being tested, instead of the 100 reported in literature ([17,18]).

Table 4.3: Cell cycling conditions.

Step name	Step time [min]	Volt [V]	Cur [A]
Rest	1		
CC_{Chg}	5	1.2	According to the electrode active area
Rest	1		
CC_{DChg}	5	0.4	According to the electrode active area

The tester starts the computations with one minute of resting time, during which no current is flown into the cell. After resting time, the battery tester charges the electrolytes for five minutes, without exceeding the maximum upper cutoff potential reported in Table 4.3. Following charging, another resting period of one minute and, then, a discharging period of five minutes. Discharging is carried out without going beyond the lower cutoff potential reported in Table 4.3. At the end of the five cycles, data about the performance of the battery (capacity, energy, voltage) were expected to appear on the screen of the computer in form of a plot.

The first experiments were carried out as follows: the positive electrolyte was prepared by dissolving potassium ferricyanide (Figure 4.10b) in 1 mol/L NaOH solution (10 mL) to afford 0.4 mol/L ferricyanide and sodium electrolyte solution. The negative electrolyte was prepared by dissolving 2,6-dihydroxyanthraquinone (Figure 4.10a) in 1 mol/L NaOH solution (10 mL) to afford 0.5 mol/L 2,6-DHAQ and sodium electrolyte solution. For all full cell studies, the electrolytes were prepared in the fully discharged state and one carbon paper for each side of the cell was employed.
In Figure 4.10, the very first samples prepared and used.

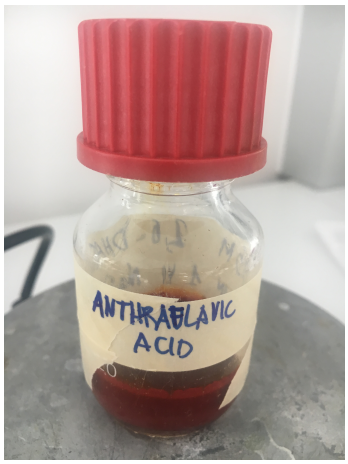

(a) 2,6-DHAQ (anthraflavic acid).

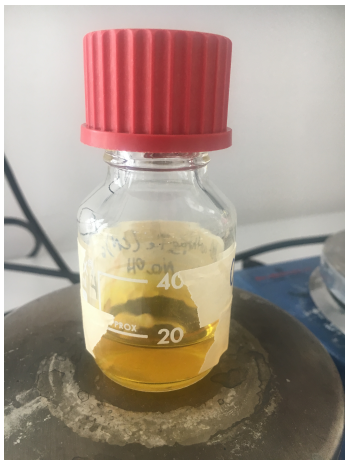

(b) $K_3Fe(CN)_6$ (Ferricyanide).

Figure 4.10: Solutions used for first cell cycling experiments.

Before testing the newly acquired cell, it was decided to run a trial investigation on an old cell setup[2] (which presents a different design as carbon papers are replaced with pieces of cloth and there is no flow field on the graphite blocks), in order to acquire more information on the functioning principles of the Neware Battery Tester and to get useful data to compare with the data eventually obtained with the new cell setup. The electrolytes used were the ones previously introduced and the current used during charging and discharging was 0.1 A. Figure 4.11 provides a general idea of the characteristics of the old cell (Figure 4.11a) and illustrates the setup during cell cycling (Figure 4.11b).

[2]In the original thesis plan, operations with an old cell setup were supposed to end with the trial just mentioned. However, more applications were introduced as necessary in order to shed some light on the unexpected results of both subsection 4.2.2 and subsubsection 4.2.3.1. For this reason, no words will be spent on describing the performance and the setup of the old cell, as a picture is considered sufficient to get a general understanding.

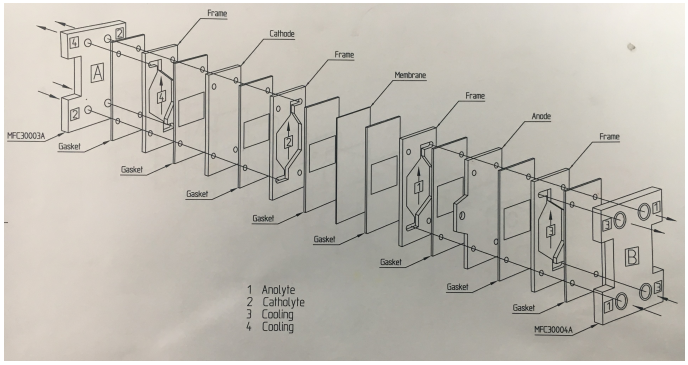

(a) Old cell blueprint.

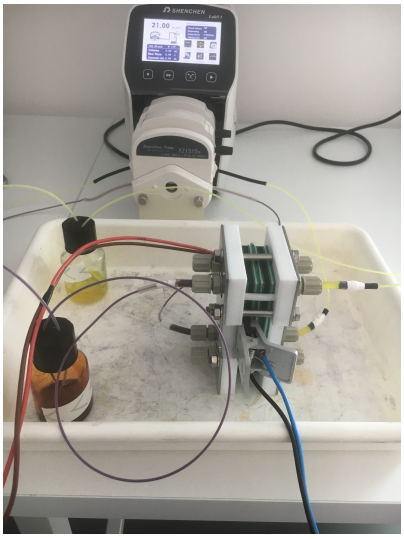

(b) Cell cycling setup.

Figure 4.11

After the trial, the investigations started on the new battery and did not proceed as expected because, even if the higher and lower cutoff potentials were set as in Table 4.3, the potentials detected from the battery tester were fluctuating between very high and very low values. This behaviour was classified as inconsistent, therefore a different approach was tried. Two different tests were run on the new cell, using freshly prepared electrolytes. For the first test, the positive electrolyte was prepared by dissolving potassium ferricyanide (Figure 4.10b) in 1 mol/L NaOH solution (10 mL or 15 mL) to afford 0.4 mol/L ferricyanide and sodium electrolyte solution. The negative electrolyte was prepared by dissolving 2,6-dihydroxyanthraquinone in 2 mol/L NaOH solution (according to *Yang et al.* [18], 1 M OH^- would have been consumed in deprotonating the quinone) (10 mL) to afford 0.5 mol/L 2,6-DHAQ and sodium electrolyte solution. For the second test, the negative electrolyte was prepared by dissolving 2,5-dihydroxy-1,4-benzoquinone (*2,5-DH-1,4-BQ*) in 2 mol/L NaOH solution (10 mL) to afford 0.5 mol/L 2,6-DHAQ and sodium electrolyte solution. However, the results obtained were far from being satisfactory as the solutions prepared with 2 mol/L NaOH were too thick to be flown inside the cell.

In reaction to the results obtained, a solid AAA rechargeable battery was tested in order to establish the correct functioning of the Neware Battery System. As this was proven to work properly, all the investigations carried out from here on were focused on finding explanations for the unforseen outcome of the cell cycling trial phase. Various

parameters were changed[3], as reported in Table 4.4, such as the number of carbon papers in each side of the cell as it was thought that an increased amount would have diminished the resistance of the battery, which was presumed to be a possible reason for the issues encountered while running the tests.

Table 4.4: Overview of the experiments carried out for cell cycling.

	Negolyte	**Solvent**	**Cell**	**Curr. [A]**	**Upper cutoff potential [V]**	**Lower cutoff potential [V]**	**Nr. of carbon papers**
I	10 mL 2,6-DHAQ	1 mol/L NaOH	Old	0.1	Not set	Not set	Cloth
II	10 mL 2,6-DHAQ	1 mol/L NaOH	New	0.625	Not set	Not set	1
III	10 mL 2,6-DHAQ	2 mol/L NaOH	New	0.625	1.7	0.7	1
IV	10 mL 2,5-DH-1,4-BQ	2 mol/L NaOH	New	0.625	1.7	0.7	1
Test on solid AAA rechargeable battery							
VI	10 mL 2,5-DH-1,4-BQ	1 mol/L NaOH	New	0.0625	1.4	0.8	1
VII	15 mL 2,5-DH-1,4-BQ 0.1 mol/L	1 mol/L NaOH	Old	0.5	1.2	0.4	Cloth
VIII	15 mL 2,5-DH-1,4-BQ 0.1 mol/L	1 mol/L NaOH	Old	0.0625	-	-	Cloth
IX	10 mL 2,5-DH-1,4-BQ	1 mol/L NaOH	New	0.0625	1.5	0.4	5
X	15 mL 2,5-DH-1,4-BQ	1 mol/L NaOH	New	0.0625	1.5	0.4	4

[3]The experiments were repeated using 0.4 mol/L $K_4[Fe(CN)_6] \times 3H_2O$ in 1 mol/L NaOH as the catholyte. The results did not differ from the ones discussed in section 5.2.

4.2.3 Limiting-current technique

The limiting-current technique is the most used method for evaluation of local and average mass-transport rates in electrochemical reactions. Investigations on mass-transport phenomena are of great interest when dealing with implementation of chemical reactions on a commercial basis, as mass-transfer can be interpreted as the migration of a component in a mixture, either within the same phase or from phase to phase, because of displacement from equilibrium [62]. In this thesis, mass-transfer phenomena were investigated in order to gain a better insight on the electrochemical reactions happening on the electrodes surface of the flow battery and to study the influence of flow and flow pattern (hydrodynamics) on the electron transfer.

The limiting-current technique is based on pushing an electrochemical reaction to the maximum possible rate, where it is limited by mass transport. On a current vs. applied potential plot, the limit is indicated by a current plateau (the limiting current). From the limiting current, the mass-transfer rate is recorded and the mass-transfer coefficient at the electrodes can be determined [69]. The maximum possible rate at which a kinetically controlled reaction proceeds at a steady state depends on the composition and transport properties of the electrolytic solution and by the hydrodynamic condition at the electrode surface [72]. When in this situation, the rate r_1 of the electrochemical process depends only on the current I (amperes), number of exchanged electrons n, and on the Faraday constant F, as in Equation 4.5 [69]:

$$r_1 = \frac{I}{n\,F} \tag{4.5}$$

In such cases, the rate of component transfer r_2 can be expressed as a function of the mass-transfer coefficient k ($\mathrm{m\,s^{-1}}$, which are those of a rate constant of a first-order heterogeneous reaction), the electrode surface A ($\mathrm{m^2}$), and the concentrations at the electrode surface (C_E; $\mathrm{kmol\,m^{-3}}$), and in the bulk solution (C_B; $\mathrm{kmol\,m^{-3}}$), as in Equation 4.6 [69]:

$$r_2 = k\,A\,(C_B - C_E) \tag{4.6}$$

where $(C_B - C_E)$ is the driving force of mass-transfer [72]. However, in the limiting-current method of measuring mass-transfer coefficients, the reacting-ion concentration at the electrode is made small by applying a sufficiently large potential

[72]. In this way, C_E becomes irrelevant and mass-transport coefficient can be determined as in Equation 4.7 [69,73]:

$$k = \frac{I_{lim}}{n\,F\,A\,C_B} \tag{4.7}$$

Finally, on a limiting-current vs. concentration plot, a linear trend is expected to appear, representing the values of mass-transfer coefficient obtained for each electrolyte concentration.

4.2.3.1 Experimental procedure

For mass-transfer investigations, a double component cell approach was used and the couple chosen was ferro/ferricyanide. Two different cells were employed during these investigations, the newly acquired setup and the old cell[4]. A volume of 50 mL of the chemical species was poured in two different glasswares and used as the feeder tanks for the flow cell. Throughout these investigation, the electrolytes were dissolved in NaOH and Na_2SO_4. The experiments were carried out by connecting a working electrode and a reference electrode to a 2 µ AUTOLAB Type III potentiostat / galvanostat (Metrohm Autolab Instruments, Netherlands) and, through clamps, to the current collectors of the battery. Once the inorganic reagents were pumped through the cell with a peristaltic pump (Shenchen LabV1, China), linear sweep galvanostatic investigations were carried out by means of the potentiostat. The linear sweep was set to collect data until a potential of 2 V was reached. Throughout the investigations, it was decided to widen the range of the potential up to 5 V. Table 4.6 illustrates the conditions applied for linear sweep of the potentials.

Table 4.5: Initial conditions for linear sweep voltammetry potentiostatic investigations.

Start potential (V)	0.000
Stop potential (V)	2 or 5
Scan rate (V/s)	0.1
Step (V)	0.002444

The new cell was first tested with the conditions shown in Table 4.6, where the reagents were dissolved in 50 mL of 1 mol/L of NaOH. The concentration of ferrocyanide was

[4]See subsection 4.2.2

double the amount the one of ferricyanide to ensure limiting reaction rate at the cathode. These investigations were repeated three times, varying the flow rates (7 mL/min, 14 mL/min and 21 mL/min).

Table 4.6: Initial experiments for linear sweep voltammetry potentiostatic investigations.

Sample	Ferricyanide [mM]	Ferrocyanide [mM]
I	2	4
II	4	8
III	6	12
IV	8	16
V	10	20

Table 4.7 shows the second set of experiments carried out on the new cell. In relation to the results of Experiment I, whose outcomes were not as expected (cfr.chapter 5), the experimental conditions were varied.

Table 4.7: Working parameters for experiments with dilution on new cell.

Experiment	Concentration [mM]	Flow rate [mL/min]	Supp. electr.
I	Dilution 10x of sample I in Table 4.6	21	1 mol/L NaOH
II	Dilution 100x of sample I in Table 4.6	21	1 mol/L NaOH
III	Dilution 200x of sample I in Table 4.6	7, 21	1 mol/L NaOH
IV	Dilution 1000x of sample I in Table 4.6	7, 21	1 mol/L NaOH

Figure 4.12 illustrates the samples employed for the experiments reported in Table 4.7.

Figure 4.12: Samples used for investigations of Table 4.7. The first two glasswares on the left are Sample I from Table 4.6, the rest is Experiment I, II, III and IV from Table 4.7.

As extensively explained in chapter 5, the outcome of these experiments did not deliver useful data for defining of mass-transfer behaviour in the newly acquired cell; as a matter of fact, the results were considered not acceptable due to what was thought to be a limit to the power of the potentiostat and due to the expected good performance of the new cell. In order to test the functionalities of the potentiostat, the investigations in Table 4.8 were carried out on an old cell setup by varying some parameters.

Table 4.8: Experiments on old cell.

Experiment	Concentration [mM]	Flow rate [mL/min]	Solvent
I	As in Table 4.6	7, 21	1 mol/L NaOH
II	Dilution 10x of sample I in Table 4.6	7	1 mol/L NaOH
III	Dilution 100x of sample I in Table 4.6	7	1 mol/L NaOH
IV	Dilution 200x of sample I in Table 4.6	7	1 mol/L NaOH
V	Dilution 1000x of sample I in Table 4.6	7	1 mol/L NaOH

Also in this case, the results were not satisfactory. Therefore, it was decided to use

sodium sulfate (Na_2SO_4) in place of sodium hydroxyde (NaOH) and run some tests only on the new cell. First, three different concentrations (1 mol/L, 0.1 mol/L and 0.001 mol/L) of sodium sulfate were tested with the potentiostat, in order to choose which concentration would give the most interpretable data. Afterwards, a new and last set of experiments was carried out, whose conditions are shown in Table 4.9.

Table 4.9: Second set of experiments on the new cell.

Experiment	Concentration [mM]	Flow rate [mL/min]	Solvent
I	As in Exp I of Table 4.6	14, 21	0.1 mol/L Na_2SO_4
II	Dilution 10x of sample I of Table 4.6	21	0.1 mol/L Na_2SO_4
III	Dilution 1000x of sample I in Table 4.6	7, 14, 21	0.1 mol/L Na_2SO_4

Figure 4.13 represents the set up used for all the investigations of mass-transfer behaviour. In particular, Figure 4.13 shows investigations employing ferricyanide (2 mM) and ferrocyanide (4 mM) in 0.1 mol/L Na_2SO_4.

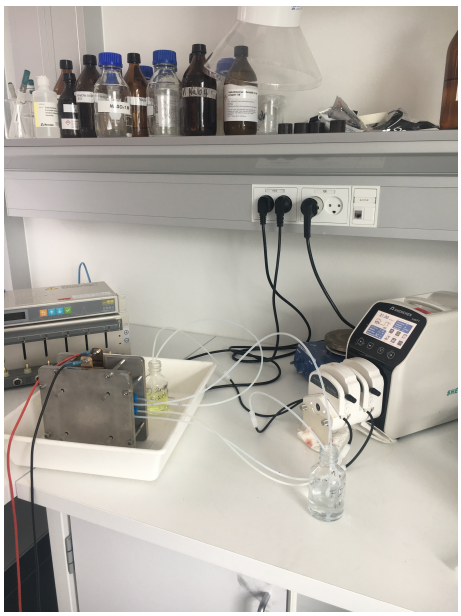

Figure 4.13: Set-up for mass-transfer investigations.

These investigations delivered negative and not interpretable results which will be discussed, together with the outcome from previous experiments, in chapter 5.

5. Results and Discussion

According to the order of chapter 4, the results obtained during the investigations will be presented and discussed.

5.1 Cyclic voltammetry

This section is organized as follows: results from the investigations on potassium ferricyanide, 2,6-DHAQ, 2-5-DH-1,4-BQ and their meaning will be extensively explained and discussed, as these are the ones that have been chosen for cell cycling. The same will not be done for the other chemical species analyzed, as equivalent considerations can be applied to them. Results of all the other electrolytes analyzed will be reported in form of a table, while the voltammograms and the relative parameters of interest are shown in section 6.1.

From the peculiar shape of the cyclic voltammograms, it is possible to get information about the reversibility of redox reactions and to calculate half-cell potentials for each chemical species and, hence, the overall battery potential. It is expected that data resulting from cyclic voltammograms of potassium ferricyanide lead to positive values for half-cell potential, whilst the half-cell potential for the quinones is expected to have negative values.

5.1.1 2,6-dihydroxyanthraquinone and ferricyanide

Figure 5.1 illustrates the results from the cyclic voltammetric investigations on 2,6-dihydroxyanthraquinone (2,6-DHAQ) and potassium ferricyanide ($K_3Fe(CN)_6$).

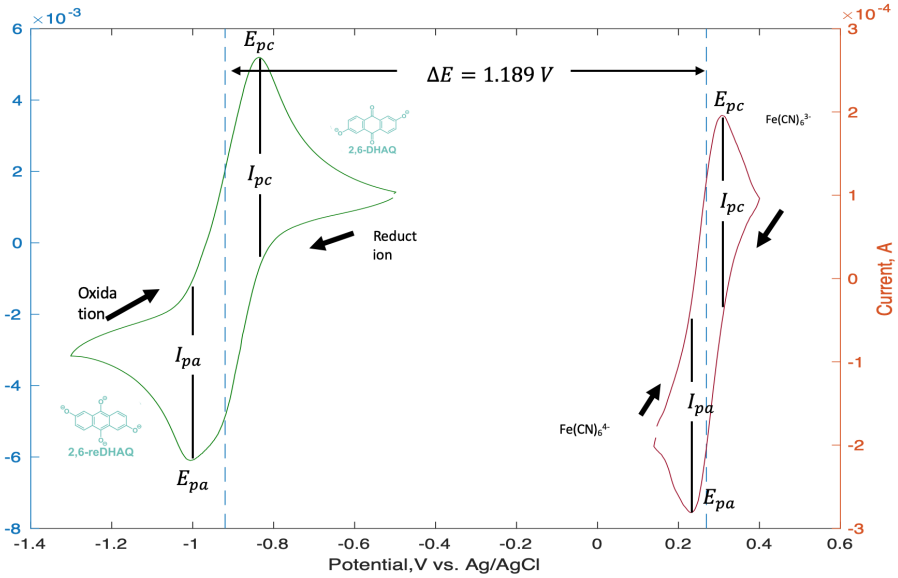

Figure 5.1: Cyclic voltammogram of 10 mM 2,6-DHAQ (green curve) and 10 mM $K_3Fe(CN)_6$ (red curve) in 1 M NaOH, scanned at 500 mV/s. The dotted lines represent the reduction potentials. Arrows indicate scan direction.

In Figure 5.1, both the voltammograms show the typical 'duck-shape', expression of redox reactions indeed happening at the electrode during scanning. As a matter of fact, the upper curve [1] on the voltammogram of potassium ferricyanide is the cathodic current appearing when Equation 5.1 takes place at the electrode:

$$Fe^{III}(CN)_6^{3-} + e^- \rightarrow Fe^{II}(CN)_6^{4-} \tag{5.1}$$

Moreover, the very sharp increase of the cathodic current, ending with a peak (E_{pc}), is due to the electrode being sufficiently strong to reduce $Fe^{III}(CN)_6^{3-}$. The presence of the peak is instead due to the decreasing in concentration of $Fe^{III}(CN)_6^{3-}$ on the electrode surface. However, as $Fe^{III}(CN)_6^{3-}$ keeps on being converted into $Fe^{II}(CN)_6^{4-}$ according to Equation 5.1, a decay of the cathodic current is visible right after E_{pc}, which ends when there is a switch in the scan direction, corresponding to the beginning of reverse scanning of the potential. The lower curve represents the effects of Equation 5.2, which is the oxidation reaction happening at the electrode:

$$Fe^{II}(CN)_6^{4-} \rightarrow Fe^{III}(CN)_6^{3-} + e^- \tag{5.2}$$

[1] In the case of potassium ferricyanide, the excitation signal first scans positively (forward scan) and then the potential is scanned in reverse. This is why anode and cathode peaks values seem reversed when calculated from the software.

As the oxidation is now generating anodic current, a sharp increase can be seen on the plot, leading to a peak (E_{pa}) caused by the depletion of $Fe^{II}(CN)_6^{4-}$ on the electrode surface. However, as the potential is still sufficiently negative to reduce $Fe^{III}(CN)_6^{3-}$, cathodic current continues even though the potential is now scanning in the positive direction. After the peak (E_{pa}), it is possible to see a decrease in anodic current, as the solution surrounding the electrode is losing $Fe^{II}(CN)_6^{4-}$.

Similar considerations can be formulated for the voltammogram on the left of the plot, belonging to 2,6-DHAQ. However, the two voltammograms show a significant difference in current signal range, therefore the two different scales on the y-axis.

Table 5.1 presents the values of peak position and peak height necessary in order to establish reversibility of the redox reactions and to calculate the overall potential of the cell (ΔE on Figure 5.1).

Table 5.1: Peaks positions and peaks heights for the two electrolytes.

	$\mathbf{E}_{pa}$	$\mathbf{E}_{pc}$	$\mathbf{i}_{pa}$	$\mathbf{i}_{pc}$
2,6-DHAQ	-0.98633	-0.8252	-0.00324	0.00351
$K_3Fe(CN)_6$	0.29541	0.2417	0,000205	-0,0001935

For potassium ferricyanide:

1. **Anodic/cathodic peak current ratio** is calculated according to Equation 4.1:

$$\frac{i_{pa}}{i_{pc}} = \frac{0,000205}{-0,0001935} \sim 1 \tag{5.3}$$

   As the peak current ratio is equal to 1, it is possible to ascertain the stability of the product on the time scale of the experiment and that potassium ferricyanide obeys a simple reversible redox coupled reaction.

2. **Number of electrons** transferred in the electrode reaction, from Equation 4.3:

$$\begin{aligned} \Delta E_p = |E_{pc} - E_{pa}| = \frac{0.059\,V}{n} &= |0.29541 - 0.2417|\,V \\ \Rightarrow 0.05371 &= \frac{0.059\,V}{n} \\ \Rightarrow n &= \frac{0.059\,V}{0.05371} = 1\,e^- \end{aligned} \tag{5.4}$$

The fact that the number of electrons transferred is equal to 1 is in line with literature ([71]), so it is possible to state that the difference between the anodic and cathodic peak potentials (ΔE_p) for the ferricyanide is indeed 57 mV at 25 °C (2.22 RT/F) and the reduction process is chemically and electrochemically reversible. Moreover, this result is in accordance with the number of electrons transferred in the reduction half-equation as expressed in Equation 5.1.

3. **Formal reduction potential** vs. Ag/AgCl reference electrode, calculated according to Equation 4.4:

$$E^{\circ\prime} = \frac{E_{pa} + E_{pc}}{2} = \frac{0.2417 + 0.29541}{2} \qquad E^{\circ\prime} = +0.269\,V \tag{5.5}$$

The value of the formal reduction potential is positive, which can also be observed from Figure 5.1, as the voltammogram lies in correspondence of positive values of the potential (x-axis). This can be interpreted, from thermodynamics, as the tendency of potassium ferricyanide to be reduced rather than oxidized.

The same calculations can be performed for 2,6-DHAQ, as in Table 5.2:

Table 5.2: Parameters for 2,6-DHAQ.

Anod./cat. peak current ratio	**Number of electrons transferred**	**Formal reduction potential**
$\frac{i_{pa}}{i_{pc}} \sim 1$	ΔE_p= 0.9 V ⇒ n = 0.3776 ∼0.5 e^-	E°′= -0.9057 V vs.Ag/AgCl

As possible to see from Table 5.1, the anodic/cathodic peak current ratio is equal to 1, showing that the redox reaction of 2,6-DHAQ should obey a simple reversible redox coupled reaction. However, the number of electrons transferred is $n \sim 0.5\,e^-$, which is in contrast with *Lin, X. et al.* ([17]) that stated a redox behaviour consistent with two one-electron reduction. Moreover, this behaviour is also inconsistent with the reduction half-equation:

$$C_{14}H_8O_4 + 2\,e^- \rightleftharpoons C_{14}H_8O_4^{2-} \tag{5.6}$$

This might indicate electron irreversibility, as there might be a slow exchange of the redox species with the WE during the cyclic voltammetry [67].

The formal reduction potential has a negative value, which indicates a tendency of this chemical species to be oxidated rather than reduced. This value is similar to the one found in a previous study [60].

After finding the formal reduction potential of the two species using their respective voltammograms, the difference of these individual species will give the theoretical cell potential, as shown in Figure 5.1. The obtained value ΔE = 1.189 V vs. Ag/AgCl is extremely close to the one reported by *Lin, X. et al.* (Δ E = 1.20 V [17]).

5.1.2 2,5-dihydroxy-1,4-benzoquinone

Figure 5.2 illustrates the duck-shaped voltammograms for 2,5-DH-1,4-BQ and $K_3Fe(CN)_6$. This quinone is characterized by one only ring in its chemical structure. From such clear peaks, the parameters of interest can be calculated using Table 5.3.

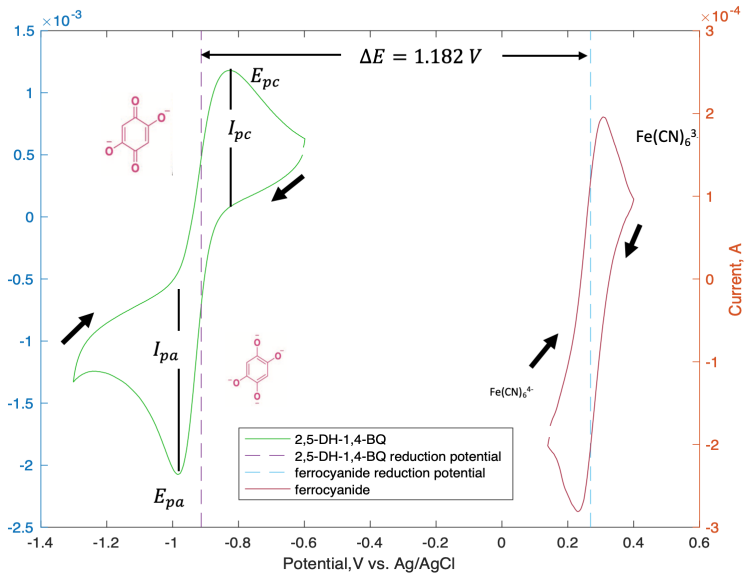

Figure 5.2: Cyclic voltammogram of 2 mM 2,5-DH-1,4-BQ (green curve) and 10 mM $K_3Fe(CN)_6$ (red curve) in 1 M NaOH, scanned at 500 mV/s. Arrows indicate scan direction.

Table 5.3: Peaks positions and peaks heights for 2,5-DH-1,4-BQ.

	E_{pa}	E_{pc}	i_{pa}	i_{pc}
2,5-DH-1,4-BQ	-0.84961	-0.97656	0,001238	-0,001705

1. **Anodic/cathodic peak current ratio** is calculated according to Equation 4.1:

$$\frac{i_{pa}}{i_{pc}} = \frac{0,001238}{-0,001705} = 0.726 \sim 1 \tag{5.7}$$

As the peak current ratio is almost equal to 1, it is possible to state the stability of the product on the time scale of the experiment and that 2,5-dihydroxy-1,4-benzoquinone obeys a simple reversible redox coupled reaction.

2. **Number of electrons** transferred in the electrode reaction, from Equation 4.3:

$$\begin{aligned} \Delta E_p = |E_{pc} - E_{pa}| = \frac{0.059\,V}{n} &= |-0.97656 - (-0.84961)|\,V \\ \Rightarrow 0.127 &= \frac{0.059\,V}{n} \\ \Rightarrow n = \frac{0.059\,V}{0.127} &= 0.465\,e^- \end{aligned} \tag{5.8}$$

The fact that the number of electrons transferred is n $\sim$ 0.5 e^- is not in line with literature ([18]), which state that the number of electrons transferred during the reduction half-equation can be expressed as in Equation 5.9:

$$C_6H_4O_4 + 2e^- \rightleftharpoons C_6H_4O_4^{-2} \tag{5.9}$$

This could indicate electron irreversibility.

3. **Formal reduction potential** vs. Ag/AgCl reference electrode, calculated according to Equation 4.4:

$$\begin{aligned} E^{\circ\prime} = \frac{E_{pa} + E_{pc}}{2} &= \frac{-0.84961 + (-0.97656)}{2} \\ E^{\circ\prime} &= -0.913\,V \end{aligned} \tag{5.10}$$

The value of the formal reduction potential is negative, which can also be observed from Figure 5.2, as the voltammogram lies in correspondence of negative values of the potential (x-axis). This can be interpreted, from thermodynamics, as the tendency of the quinone to be oxidized rather than reduced, during redox reactions. The calculated value of formal reduction potential is the same as the one determined by [18]. From the value of half-cell formal potential of both 2,5-DH-1,4-BQ and ferricyanide, it is possible to calculate the theoretical cell

potential, as shown in Figure 5.2. The obtained value ΔE = 1.182 V is very close to the one observed by *Yang et al.* (1,21 V [18]).

5.1.3 Excluded quinones

Table 5.4 shows the calculated values of theoretical cell potential for the other quinones analyzed. According to [17, 18], the targeted cell potential is 1.2 V. The following quinones delivered smaller cell potentials when coupled with potassium ferricyanide; hence, they have been discarded from further applications.

Table 5.4: Values of theoretical cell potential for quinones non further used.

Quinone	ΔE
1,8-DHAQ	1.055 V
1,5-DHAQ	1.008 V
1-HA-9,10-Q	0.965 V
1,4-NQ	1.085 V
TF-1,4-BQ	1.085 V

5.2 Cell cycling

Cell cycling experiments were carried out on both the new cell and the old one. The results are presented following the order of Table 4.4.

5.2.1 Experiment I

Figure 5.3 shows the results for cell cycling of the old battery setup through 5 cycles recorded at 0.1 A/cm^2.

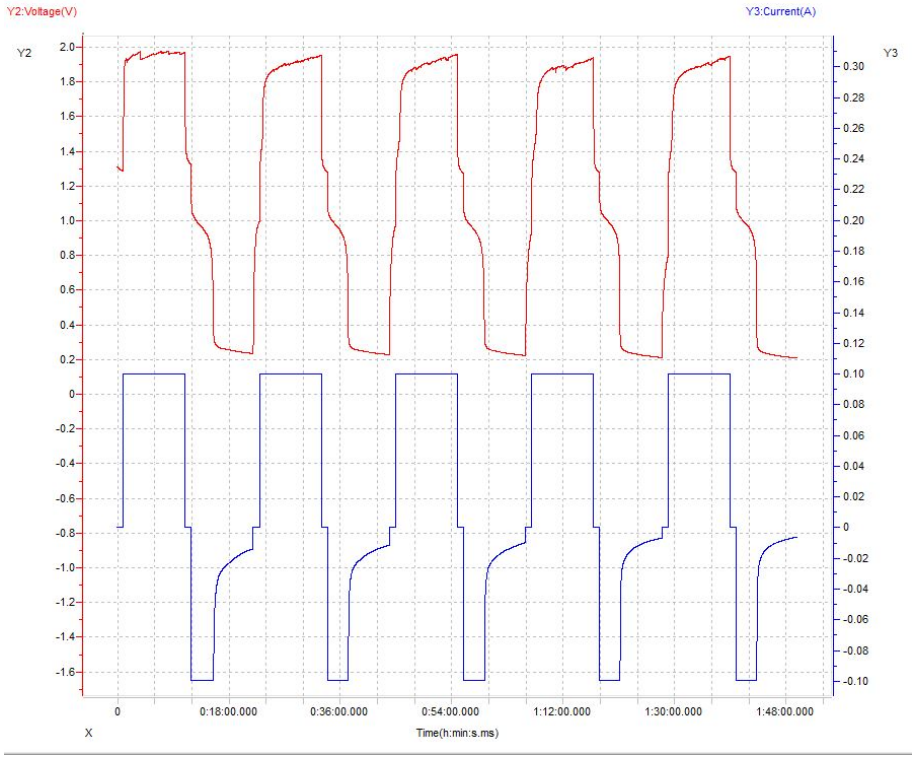

Figure 5.3: Representative voltage vs. time and current vs. time curves during 5 charge-discharge cycles at 0.1 A/cm^2

It is possible to see that the results seem to confirm the investigations carried out by *Busuic et al.* [60] on the same cell and with the same electrolytes, but using a different setup. Lower and upper cutoff voltages in Figure 5.3 are 0.2 V and 2 V, respectively, whilst in the previous work they where found out to be 0.5 V and 1.5 V, respectively. Moreover, the voltage drops rapidly but slows down for all the cycles when reaching the range between 1.30 V and 0.8 V, giving the appearance of a small "bump", as also observed by [60]. Furthermore, as the experiment was carried out with a constant current value, the lower part of Figure 5.3 is interpreted as the plot of internal resistance (Ω) vs. time, which appears to be the same as previous studies [60]. However, investigations on the old cell did not proceed in depth, as their only aim was to provide data for comparison and to state the good functioning of the battery tester, which they did.

5.2.2 Experiment II

In Figure 5.4 are the results for the cell cycling carried out on the new battery. The cutoff potentials were not set.

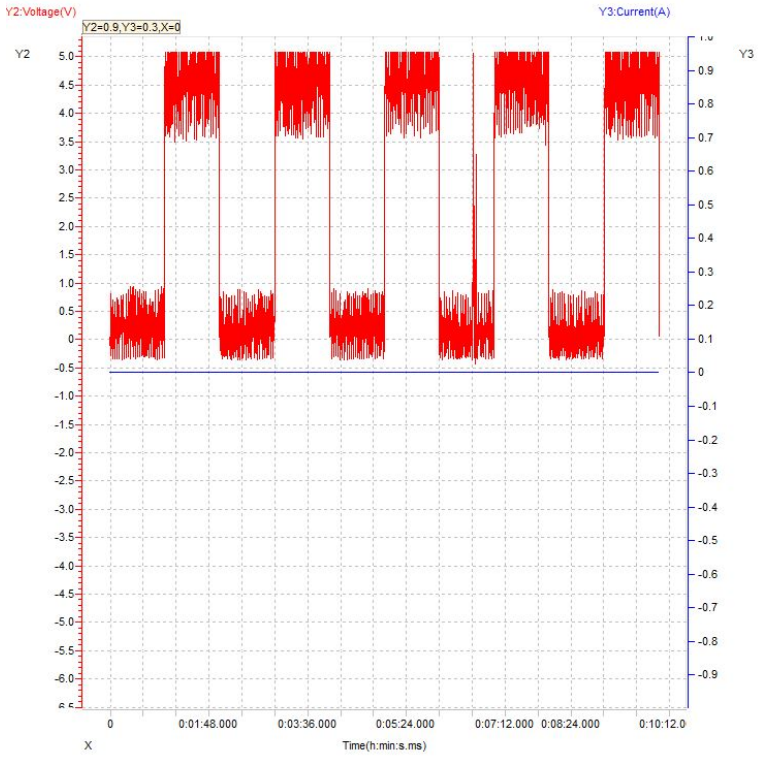

Figure 5.4: New cell representative voltage vs. time curves during 5 charge-discharge cycles at 0.625 A/cm^2.

As possible to see from the figure, the cell seems not to be cycled at all. The values of lower and upper cutoff are the minimum and maximum values reachable for the battery tester. Moreover, a plot of current vs. time is missing in the lower part of Figure 5.4, meaning that current was not flowing into the battery. Possible explanations for these unforeseen results were thought to be related to an incorrect assembling of the battery, to unreactive electrolytic solutions or, more likely, to no redox reaction happening inside the cell. If no redox reaction was happening, the potential recorded on Figure 5.4 is the one belonging to the battery tester itself. After the test, however, it was noted that the color of potassium ferricyanide changed from light yellow (before test) to dark green. Usually the color changing of an electrolyte solution is due to redox reactions taking place and to different oxidation states of the compounds; hence, the fact that the electrolyte changed color, was a proof that some kind of reaction was happening into the cell during charge and discharge. Moreover, a further anomaly was observed on the screen of the computer prior to cell cycling: when the cable connecting the cell to the tester was in place, the potential was not fixed, but rather fluctuating between very negative and positive values.

5.2.3 Experiments III and IV

When trying to cycle the cell with both 2,6-DHAQ and 2,5-DH-1,4-BQ dissolved in 2 M NaOH, some issues occurred and it was not possible to actually run cell cycling experiments. Once the battery was ready, the pump was switched on and the electrolytes started flowing. However, despite the flow rate for the species was set to 21 mL/min, it seemed like the flow of the quinone solutions was considerably slower than the one of potassium ferricyanide. The quinones were so thick to be stuck between the graphite blocks (Figure 5.5a) and the carbon papers (Figure 5.5b).

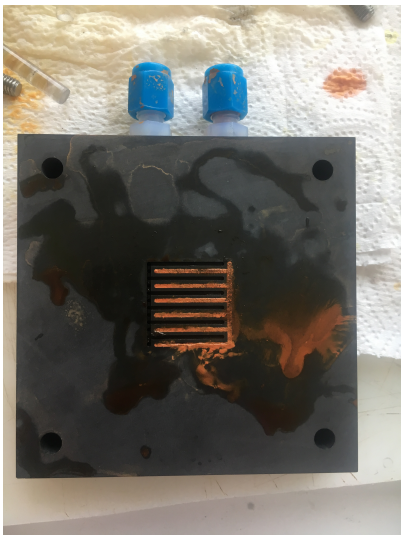

(a) Electrolytes stuck in the flow field channels.

(b) Carbon papers impregnated with very thick electrolytes.

Figure 5.5

According to the outcome of these investigations, the solubility of the quinones in 2 M NaOH decreases too much and the electrolytes are, therefore, inoperable. This is in contrast with the studies carried out by [18].

5.2.4 Experiment with solid state battery

As the values of potential recorded on the screen of the computer were fluctuating when the cell was connected to the tester, even if the cell was not being cycled and the upper and lower cutoff potential values were set, tests on a solid battery were performed to try to figure out if the problem was due to the tester itself, to the cable or to the cell. For this reason, the cable with the clamps was connected to pieces of copper and these pieces were, in turn, fixed to the anode and cathode of the solid battery. When in this

situation, the voltage could be seen not to fluctuate, so it was decided that the cable was functioning perfectly. Moreover, the solid AAA rechargeable battery was cycled when placed in the dedicated spaces on the battery tester. In this case, upper and lower cutoff potentials were set, and the battery tester recognized the value of potential of 1,2 V automatically (that is the value of potential written on the solid battery). In light of this, it was decided that the problem was related to the new cell setup.

5.2.5 Experiment VI

From now on, the experiments were carried out with the aim of understanding the peculiar and unexpected behaviour of the new battery setup. In the following trial, the value of the current was reduced to ten times the original one, the number of carbon papers was unaltered and upper and lower cutoff potentials were set.

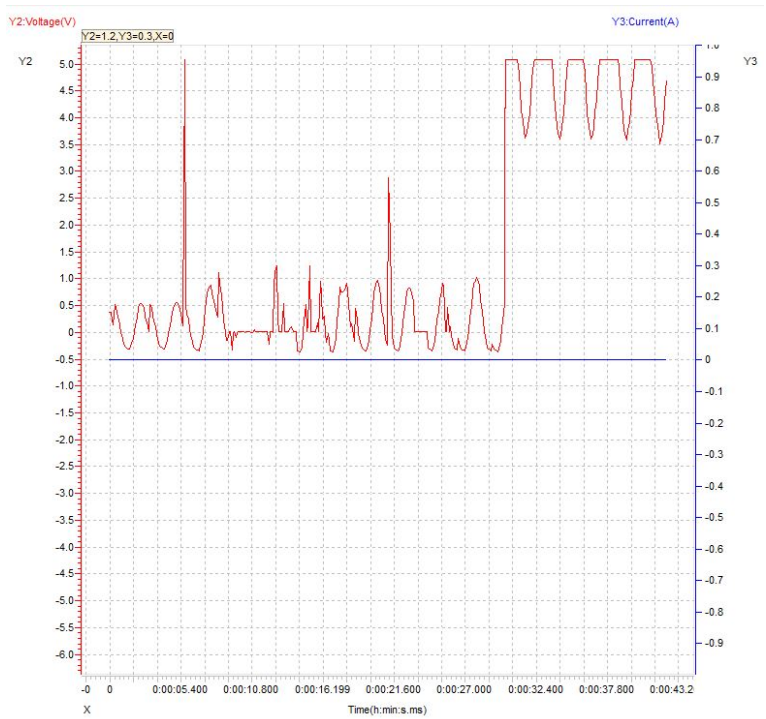

Figure 5.6: New cell representative voltage vs. time curves during attempted charge-discharge cycles at 0.0625 A/cm^2.

As possible to see from Figure 5.6, the voltage vs. time curves were following a trend that is hard to interpret. The time range of the computation ends at 43 sec, meaning that the curves belong to the resting phase. Compared to Figure 5.3, where the resting phase is characterized by straight curves, the curves observed on Figure 5.6 are inconsistent

with a typical cell cycling experiment ([17,18,60]). Moreover, an anomaly was observed during the experiment: after the resting time of one minute, the battery tester was unable to start the charging phase, and the battery was in a constant state of rest. More precisely, during the resting phase, an orange light switches on on the battery tester, that turns into green during charging phase. During this investigation, however, the orange light could never turn into green. As of today, this outcome still remains unexplained.

5.2.6 Experiments VII and VIII

In a further attempt to explain the peculiar outcome of the previous experiments, and to state with 100 % confidence that the issues developing were exclusively related to the new cell setup, experiments were again carried out on the old cell, using 2,5-DH-1,4-BQ. However, the results of these experiments were unforeseen.

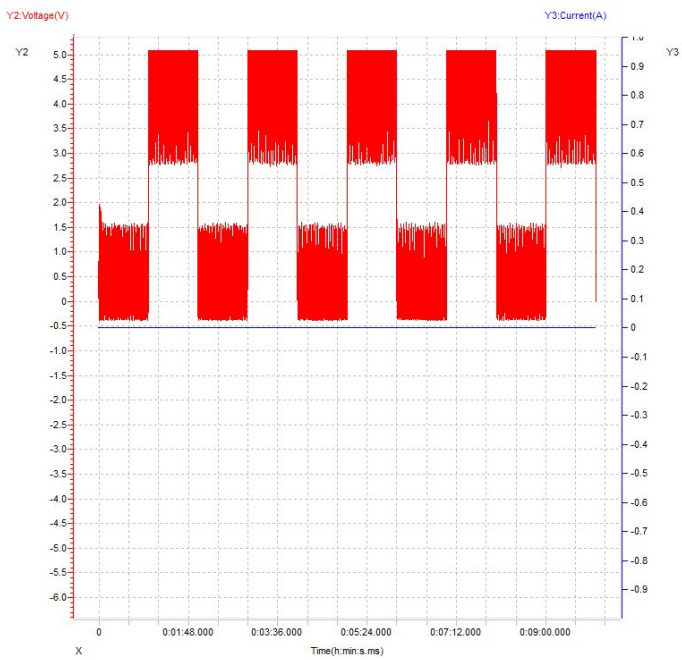

Figure 5.7: Voltage vs. time curves during attempted charge-discharge cycles at 0.0625 A/cm^2 on the old cell.

Figure 5.7 is relative to Experiment VIII in Table 4.4, where no lower and upper cutoff potentials were set. The results are the same as in Figure 5.4, as the tester seems to record its internal potential, or its internal performances. The maximum value of potential that the Neware Battery Testing System can reach is 5 V, and in Figure 5.7 that is the potential observed. Regarding the results from Experiment VII of Table 4.4, inserting cutoff

potential values blocked the tester from being able to start the charging-discharging cycles after the resting time.

5.2.7 Experiments IX and X

New experiments were performed using an increased number of carbon papers, as it was thought that the reason for the behaviour observed in subsection 5.2.5 was due to a high internal cell resistance, which could have restricted the current from flowing. By using more carbon papers on each side of the battery, the resistance could have been lowered.

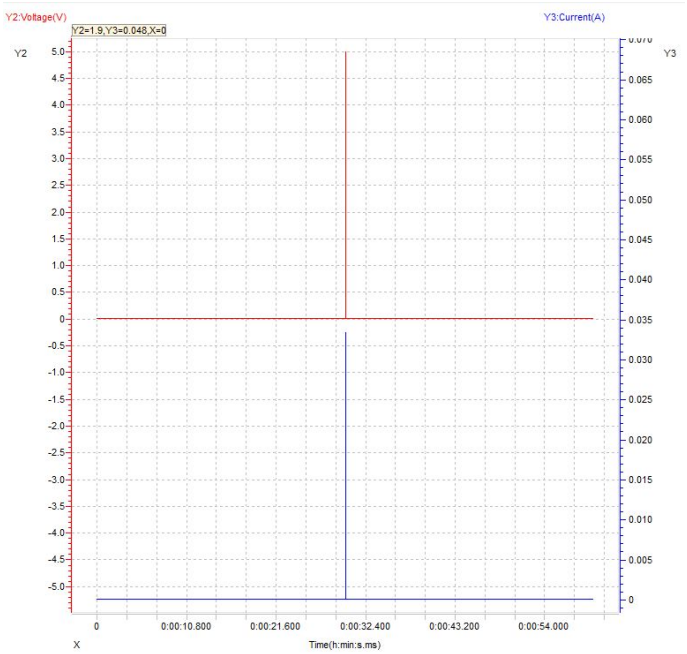

Figure 5.8: Attempted charge-discharge cycles at 0.0625 A/cm^2 with increased number of carbon papers.

As possible to see from Figure 5.8, during resting time (until 54 sec), the setup seemed to work fine, except for the signal visible around 32 sec. However, after the one minute resting time passed, the same issue encountered in subsection 5.2.5 appeared and it was impossible to run charging and discharging cycles. Therefore, even if not reported in Table 4.4, this exact experiment was tried again without setting cutoff potentials. During charging and discharging, not only very high potential values were reached, but also the current registered was not 0.0625 A, as manually set in the working conditions of the battery tester. During this investigation, it was impossible to control the battery tester, but no explanation has been found. Moreover, after disassembling the battery,

cuts on the Nafion®212 membrane were visible. This could be due to a too high number of carbon papers on both sides of the cell, as the shape of the cuts followed the frame of the carbon papers, which is also the frame of the flow fields channel. However, for sake of clearance and understanding, a multimeter was employed during another attempted charge and discharge investigation. With a circuit completed by the ammeter being connected in series with the cell, a current of 4.4 μA was registered, revealing a cell resistance of 38 $K\Omega$. It is not clear yet if such a high value of resistance is due to the cell itself, or to the chemical species employed during cell cycling.

5.3 Limiting-current technique

5.3.1 Initial experiments on the new cell

The following results are relative to the species in Table 4.6, where the reagents are dissolved in 50 mL of 1 mol/L of NaOH.

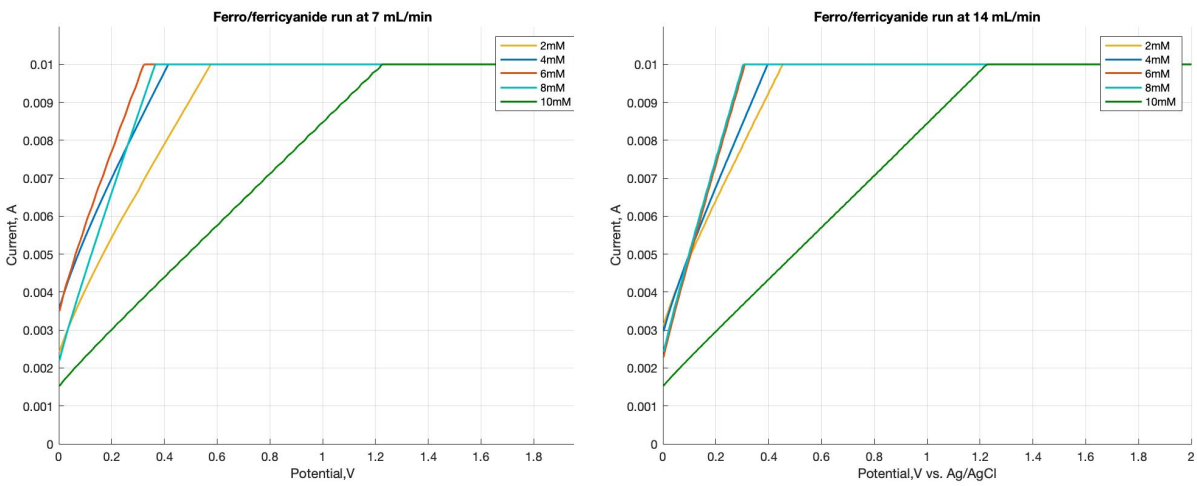

(a) **(b)**

Figure 5.9: Linear sweep voltammograms with a scan rate of 0.1 V/s. The legend is for the concentrations of ferricyanide.

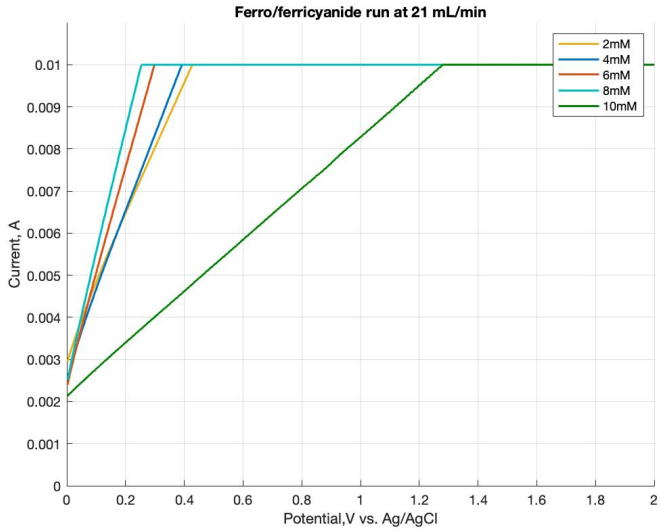

Figure 5.10: Linear sweep voltammogram with a scan rate of 0.1 V/s. The legend is for the concentrations of ferricyanide.

Figure 5.9a illustrates mass-transfer rates when the electrolytes are pumped through the new cell with a rate of 7 mL/min. All the curves follow the same trend, sharply reaching the maximum current value 0.01 A. Moreover, there seems not to be any relationship between the concentration of the electrolytes and the velocity with which the maximum current value is reached, as the green curve (higher concentration of ferricyanide) is the slowest, as instead observed by [73]. According to the results, the new cell seemed to be very efficient in terms of mass-transfer. However, the maximum current value reached does not appear to be a plateu, but rather a limit in the power of the potentiostat. Figure 5.9b and Figure 5.10 show the same trends as in Figure 5.9a, despite the flow rates of the electrolytes are different.

5.3.2 Experiments on new cell with dilution

As the results from the first investigations (cfr. subsection 5.3.1) did not show any valuable information about mass-transfer rate, therefore not allowing calculations of mass-transfer coefficients, dilution of the electrolytes was done in order to overcome the issue with the maximum current range. Information about the dilution factors can be found in Table 4.7.

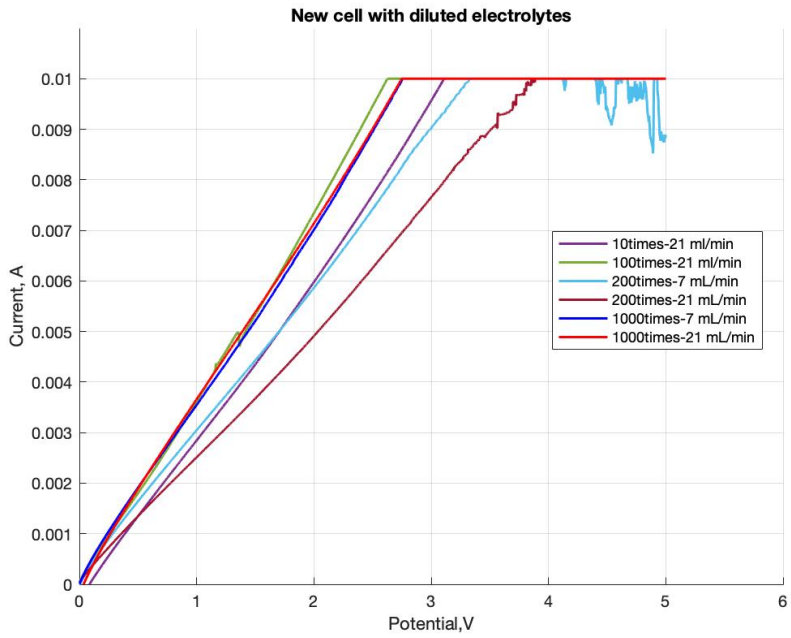

Figure 5.11: Investigations of mass transfer on the new cell with diluted electrolytes.

These results in Figure 5.11 represent a slight improvement compared to the ones previously discussed, as it seems that the potentiostat carries out a better control of the reaction. From Figure 5.11, it is possible to see that the starting value of the current is zero, and that the curves show less sharp trends. However, the current range is still not high enough to allow for optimal mass-transfer rate investigations, therefore a plateau is still not clearly visible. Overall, these results do not match the expectations, as the curve displayed in Figure 5.11 is very far from what is reported in literature [73].

5.3.3 Experiments on the old cell.

The old cell was employed when the experiments carried out on the new cell with the diluted electrolytes still showed problems with the maximum current rage, as an overload of current appeared at 0.01 A. It was thought that, as the old cell was not optimized, a worst mass-transfer was achievable and, therefore, the possibility of detecting a current plateau was expected. In Figure 5.12 are the results of the investigations carried out as in Table 4.8.

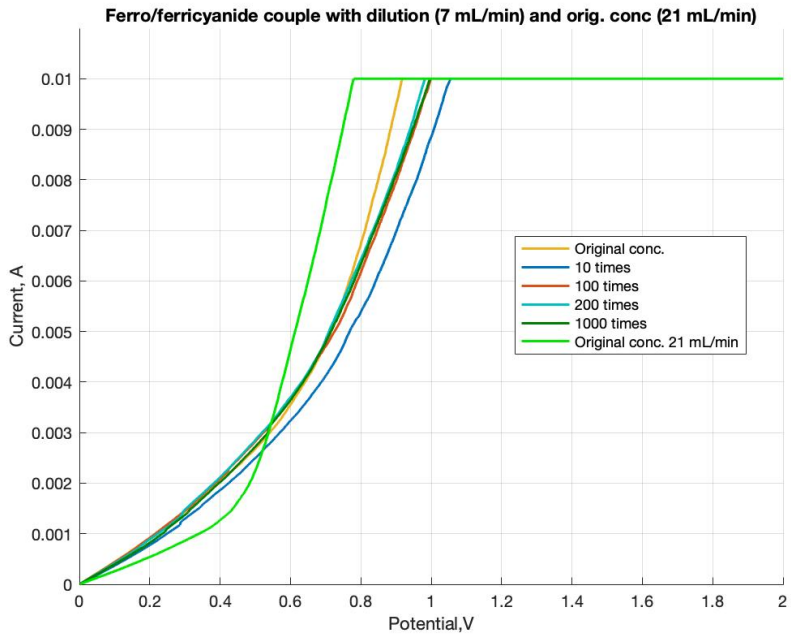

Figure 5.12: Investigations of mass transfer on the old cell. Dilution were made of the first concentration couple of the electrolytes.

As possible to see from the figure, the mass-transfer behavior for the old cell presents a different trend than the one observed in Figure 5.11, as the maximum current value is reached following a parabolic trend. A parabolic trend is not at all what the polarization curves for mass-transfer investigations should look like. Moreover, also in this case, the concentration of electrolytes seems not to affect the rate of mass-transfer, as the blue curve, indicating a dilution by a factor of 10 of the original concentration, is the slowest curve. However, it seems like the behaviour of the mass-transfer rate for the old cell is completely random. Anyway, from the figure becomes clear that the mass-transfer rate could not be completely investigated as the maximum current value of 0.01 A represents again a value of current overload.

5.3.4 Experiments on mass-transfer with Na_2SO_4

As all the trials carried out did not lead to a useful diagram able to determine the limiting current needed to calculate mass-transport coefficients, it was decided to repeat the investigations using Na_2SO_4 as a the supporting electrolyte, instead of NaOH. Extensive literature data have proven Na_2SO_4 to be a good supporting electrolyte, able to reduce mass transport caused by migration flows so that the current can be generated solely from diffusion events [74]. The conditions for the experiments are reported in Table 4.9.

5.3.4.1 Na_2SO_4

In Figure 5.13 results from linear sweep voltammetry on three different concentrations of the supporting electrolyte.

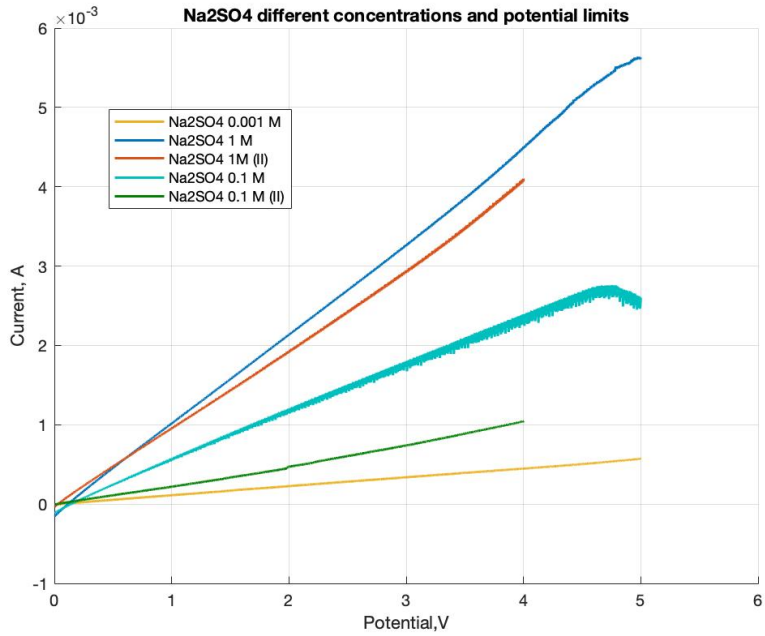

Figure 5.13: Linear sweep voltammetry of three different Na_2SO_4 concentrations.

From the figure, it becomes clear that a maximum upper potential range of 4 V or 5 V is not enough to follow the evolution of the electrochemical behavior of the supporting electrolyte. However, not much could be done about that as the 2 µ AUTOLAB Type III potentiostat / galvanostat (Metrohm Autolab Instruments, Netherlands) cannot reach higher values of potential. Anyway, from the plot a trend is visible as higher concentrations of Na_2SO_4 reach the maximum value of current with a sharper slope. Moreover, it has to be noted that the y-axis shows a different value of maximum current range (6×10^{-3} A), which is considerably smaller than the one previously observed. This was interpreted as a success, meaning that addition of Na_2SO_4 enhances the performance of the potentiostat, as conducting solutions make it easy for electrochemistry to happen. According to Figure 5.13, it was chosen to use Na_2SO_4 0.1 M for the next investigations, as a slight plateau seems to be reached around 3×10^{-3} A.

5.3.4.2 Mass-transfer on new cell

The following was the last attempt done in order to obtain information about mass-transfer coefficients. As possible to see from Figure 5.14, the trend shown is not to be considered as informative at all, as very far from expectations ([73]).

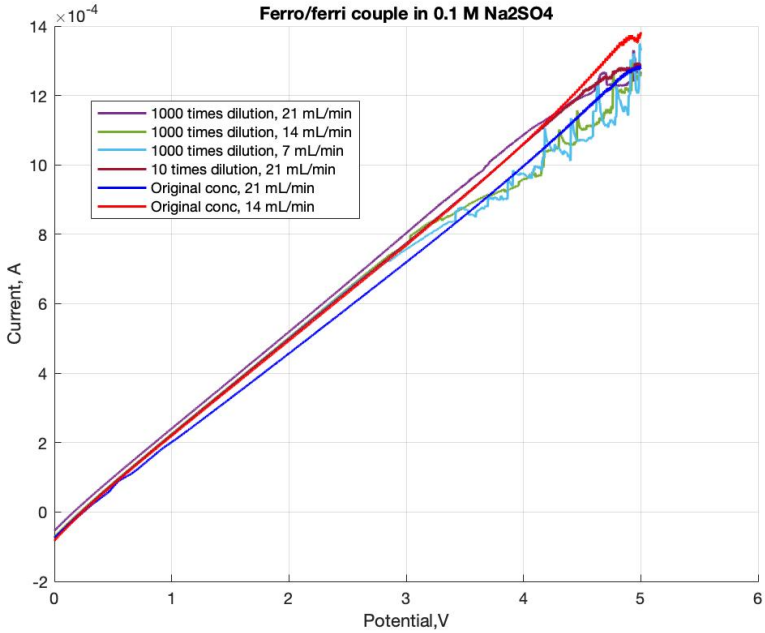

Figure 5.14: Mass-transfer investigations on new cell with 0.1 M Na_2SO_4 as the supporting electrolyte.

However, it is interesting to note how the range of the current is higher than in Figure 5.11, but still no current plateau can be reached. A possible explanation for the observed trends is that the new cell is very excellent in terms of mass transfer, as sharp straight curves replaced the typical polarization ones for mass-transfer investigations; however, values of mass-transfer coefficients could not be obtained as the limiting-current plateau was never reached, most likely because of the presence of the membrane. In fact, as reported in literature ([75]), the plateau in the current-voltage curve can be observed only in simple electrochemical cells in which a single solution-filled channel is limited by two electrodes. In these cases, the diffusion-limited current density is univocally determined by the plateau.

6. Conclusions

The main aim of this experimental work was to investigate the influence of cell design and hydrodynamics on the performance a new redox flow battery present in the laboratories of the Section of Chemical Engineering at Aalborg University in Esbjerg.

In order to identify the most performing quinones to operate in the newly acquired cell, cyclic voltammetry investigations were carried out, as they provide information about the reversibility of a redox reaction, about electron stoichiometry of a system and about the formal reduction potential. In light of the results obtained, 2,6-dihydroxyanthraquinone and 2,5-dihydroxy-1,4-benzoquinone were chosen as able to deliver theoretical cell potentials of 1.189 V and 1.182 V, respectively, when coupled with potassium ferricyanide.

Investigations on the performance of the new battery resulted impossible to be carried out, as the newly acquired cell was not properly functioning when redox species were flown through it. It was impossible to run charge and discharge cycles when the cutoff potentials were set, as the battery tester did not allow computations. Furthermore, charge and discharge cycles carried out without manually setting cutoff potential values turned out to register the internal potential of the battery testing system station. As the internal resistance of the battery was measured to be 38 KΩ, more investigations need to be performed on the chemical species employed as electrolytes and on the cell design.

Obtaining values of mass-transfer coefficients to gain information about influence of flow and flow pattern on the electron transfer through limiting-current technique, resulted not to be feasible. The potentiostat was showing a clear working limit and, more likely, these kind of investigations cannot be performed when ion-exchange membranes are present.

Bibliography

[1] BP. Bp energy outlook - 2018 edition. https://www.bp.com/content/dam/bp/business-sites/en/global/corporate/pdfs/energy-economics/energy-outlook/bp-energy-outlook-2018.pdf, 2018. Accessed: 9-05-2019.

[2] Goodenough, J. B. and Youngsik Kim. Challenges for rechargeable li batteries. *Chemistry of Materials*, 22(3):587–603, 2010.

[3] Renewables 2018 – market analysis and forecast from 2018 to 2023. https://www.iea.org/renewables2018/. Accessed: 8-05-2019.

[4] Luing, P. et al. Progress in redox flow batteries, remaining challenges and their applications in energy storage. *The Royal Society of Chemistry Advance*, 2:10125–10156, 2012.

[5] Dong et al. Environmentally-friendly aqueous li (or na)-ion battery with fast electrode kinetics and super-long life. *Science Advances*, 2(1), 2016.

[6] Grigorii L. Soloveichik. Flow batteries: Current status and trends. *Chemical Reviews*, 2014.

[7] Eurostat Newsrelease. Share of renewable energy in the eu up to 17.5 % in 2017. https://ec.europa.eu/eurostat/documents/2995521/9571695/8-12022019-AP-EN.pdf/b7d237c1-ccea-4adc-a0ba-45e13602b428, 2019. Accessed: 8-05-2019.

[8] Danish Energy Agency. The danish energy model – innovative, efficient and sustainable. https://ens.dk/en. Accessed: 8-05-2019.

[9] D.P.Zafirakis. Overview of energy storage technologies for renewable energy systems. In The editor, editor, *Stand-Alone and Hybrid Wind Energy Systems - Technology, Energy Storage and Applications*, chapter 2, pages 29–80. Woodhead Publishing Limited, 2010.

[10] Chalamala, B. R. et al. Redox flow batteries: An engineering perspective. *Proceedings of the IEEE*, 102(6):976 – 999, June 2014.

[11] Sum, E. et al. Investigation of the v(v)/v(iv) system for use in the positive half-cell of a redox battery. *Journal of Power Sources*, 16:85–95, 1985.

[12] Wang, W. et al. Recent progress in redox - flow battery research and development. *Advanced Functional Materials*, 23(8):970–986, 2012.

[13] Li, L. et al. A stable vanadium redox-flow battery with high energy density for large-scale energy storage. *Advanced Energy Materials*, 1:394–400, 2011.

[14] Chen, H. et al. Recent progress in organic redox flow batteries: Active materials, electrolytes and membranes. *Journal of Energy Chemistry*, 27(5):1304–1325, September 2018.

[15] Organic-based aqueous flow batteries for massive electrical energy storage'. presentation by m. aziz at princeton university. `http://nuweb9.neu.edu/mres/wp-content/uploads/2014/11/Michael-Aziz-presentation.pdf`, 10 2014.

[16] Grid energy storage, u.s. department of energy, 2013. `https://www.energy.gov/oe/downloads/grid-energy-storage-december-2013`, 2013.

[17] Lin, K. et al. Alkaline quinone flow battery. *Science*, 6255(349):1529–1532, September 2015.

[18] Yang Zhengjin. Alkaline benzoquinone aqueous flow battery for large-scale storage of electrical energy. *Advanced Energy Materials*, pages 1702056–1702056, September 2017.

[19] Huskinson, B. et al. A metal-free organic–inorganic aqueous flow battery. *Nature*, 505(12909):195–210, January 2014.

[20] Hazza, A. et al. A novel flow battery — a lead acid battery based on an electrolyte with soluble lead(ii). part i: Preliminary studies. *Physical Chemistry Chemical Physics*, 6:1773–1778, 2005.

[21] Joseph, G.G.II et al. High performance flow battery, October 2011. US Patent 20110244277 A1.

[22] Stern, N. Stern review: The economics of climate change. *HM Treasury*, 2006.

[23] Chicco, G. and P. Mancarella. Distributed multi-generation: A comprehensive view. *Renewable and Sustainable Energy Reviews*, 13:535–551, 2009.

[24] Pepermans, G. et al. Distributed generation: definition, benefits and issues. *Energy Policy*, 33:787–798, 2005.

[25] Tellidou, A.C. and Bakirtzis A.G. Demand response in electricity markets. Conference: Power Engineering Society General Meeting, 2007. IEEE, 7 2007.

[26] Amiryar, M.E. and Keith R. Pullen. A review of flywheel energy storage system technologies and their applications. *Applied Sciences*, 7(286):1–21, 2017.

[27] Zhang, H. *Large-Scale Energy Storage: An Overview*, chapter 1, pages 1–42. CRC Press. Taylor & Francis Group, 6000 Broken Sound Parkway NW-Suite 300. Boca Raton, FL, 2018.

[28] Dehghani-Sanij, A.R. et al. Study of energy storage systems and environmental challenges of batteries. *Renewable and Sustainable Energy Reviews*, 104:192–208, April 2019.

[29] Asian Development Bank, 6 ADB Avenue, Mandaluyong City, 1550 Metro Manila, Philippines. *Handbook On Battery Energy Storage System*, 12 2018.

[30] Makansi, J. and J. Abboud. Energy storage - the missing link in the electricity value chain. *Energy Storage Council*, 2002.

[31] Wang, W. et al. Introduction to redox flow batteries. In Jiujun Zhabg, editor, *Redox Flow Batteries - Fundamentals and Applications*, chapter 8, pages 43–76. CRC Press - Taylor & Francis Group, 6000 Broken Sound Parkway, NW Suite 300, Boca Raton, FL 33487, 2018.

[32] Zhang, D. et al. Design of flow battery. In *Reactor and Process Design in Sustainable Energy Technology*, chapter 3, pages 61–97. Elsevier B.V., Radarweg 29, PO Box 211, 1000 AE Amsterdam, The Netherlands The Boulevard, Langford Lane, Kidlington, Oxford OX5 1GB, UK, 2014. `http://dx.doi.org/10.1016/B978-0-444-59566-9.00003-X`.

[33] Alotto, P. et al. Redox flow batteries for the storage of renewable energy: A review. *Renewable and Sustainable Energy Reviews*, 29:325–335, January 2014.

[34] Su, L. et al. Recent developments and trends in redox flow batteries. In Zhengcheng Zhang and ShengShuiZhang, editors, *Rechargeable Batteries - Materials, Technologies and New Trends*, chapter 23, pages 673–712. Springer.

[35] Pezeshki, A.M. et al. Elucidating effects of cell architecture, electrode material, and solution composition on overpotentials in redox - flow batteries. *Electrochimica Acta*, 229:261–270, 2017.

[36] Kok, M.D.R. et al. Multiphysics simulation of the flow battery cathode: Cell architecture and electrode optimization. *Journal of Electrochemical Society*, 163:A1408–A1419, 2016.

[37] Cao, R. et al. Organic cathode materials for rechargeable batteries. In Zhengcheng Zhang and ShengShuiZhang, editors, *Rechargeable Batteries - Materials, Technologies and New Trends*, chapter 23, pages 637–672. Springer.

[38] Zhou, X.L. et al. A highly permeable and enhanced surface area carbon-cloth electrode for vanadium redox - flow batteries. *Journal of Power Sources*, 329:247–254, October 2016.

[39] Li, J. Cell design and electrode material for all vanadium redox - flow battery. Master's thesis, University of Calgary, Alberta, 2018.

[40] Viswanathan, V. et al. Cost and performance model for redox flow batteries. *Journal of Power Sources*, 247:1040–1051, February 2014.

[41] Chakrabarti, M.H. et al. Application of carbon materials in redox flow batteries. *Journal of Power Sources*, 253:150–166, January 2014.

[42] Kim, K.J. et al. A technology review of electrodes and reaction mechanisms in vanadium redox flow batteries. *Journal of Material Chemistry*, 3:16913–16933, June 2015.

[43] Trevor J. Davies and Joseph J. Tummino. High-performance vanadium redox flow batteries with graphite felt electrodes. *Journal of Carbon Research*, 4(1:8), January 2018.

[44] Lu, W. and D.D.L. Chung. A comparative study of carbons for use as an electrically conducting additive in the manganese dioxide cathode of an electrochemical cell. *Carbon*, 40(3):447–449, March 2002.

[45] Parasuraman, A. et al. Review of material research and development for vanadium redox flow applications. *Electrochimica Acta*, 101:27–40, 2013.

[46] Schmidt-Rohr, K. and Chen Q. Parallel cylindrical water nanochannels in nafion fuel-cell membranes. *Nature Materials*, 7:75–83, December 2008.

[47] Kahraman, H. et Orhan M.F. Flow field bipolar plates in a proton exchange membrane fuel cell: Analysis & modeling. *Energy Conversion Management*, pages 363–384, 2016.

[48] Han, W. et al. Batch dark fermentation from enzymatic hydrolyzed food waste for hydrogen production. *Bioresource Technology*, 191:24–29, September 2015.

[49] Hobrecht, M.A. and L. H. Thaller. Design flexibility of redox flow systems. Intersociety Energy Conversion Engineering Conference, Los Angeles, CA, USA, NASA, 7 1982. Rep. N82-31459, Aug. 8–13.

[50] Sangwon Kim. Vanadium redox flow batteries: Electrochemical engineering. In Dr. M. Taha Demirkan, editor, *Energy Storage Devices*. IntechOpen, April 2019.

[51] Ke, X. et al. Rechargeable redox flow batteries: flow fields, stacks and design considerations. *Chemical Society Review*, 23(47):8721–8743, October 2018.

[52] El-Najjar, N. et al. The chemical and biological activities of quinones: overview and implications in analytical detection. *Phytochemistry Reviews*, 10(3):353–370, April 2011.

[53] Hu, B. et al. Long-cycling aqueous organic redox flow battery (aorfb) toward sustainable and safe energy storage. *Journal of the American Chemical Society*, 139(3):1207–1214, 2017.

[54] Chen, Q. et al. Cycling analysis of a quinone-bromide redox flow battery. *Journal of The Electrochemical Society*, 163(1), 2016.

[55] Minori Uchimiya and Alan T. Stone. Reversible redox chemistry of quinones: Impact on biogeochemical cycles. *Chemosphere*, 77(4):451–458, August 2009.

[56] Sarathi, G.P. et al. Electrochemical reduction of quinones in different media: A review. *International Journal of Electrochemistry*, 2011, August 2010.

[57] Sanchez,Q.M. et al. Voltammetry of quinones in unbuffered aqueous solution: Reassessing the roles of proton transfer and hydrogen bonding in the aqueous electrochemistry of quinones. *Journal of the American Chemical Society*, 129(42):12847–12856, June 2007.

[58] Huskinson, B. et al. Organic-based aqueous flow batteries for massive electrical energy storage. `http://nuweb9.neu.edu/mres/wp-content/uploads/2014/11/Michael-Aziz-presentation.pdf`, August 2014. 2nd Int'I Conference on Multiscale Renewable Energy Storage, Northeastern University.

[59] Musso, H. Oxidative coupling of phenols. In Battersby A.R. Taylor, W.I., editor, *Organic substances of natural origin.*, volume 1, pages 1–84. Marcel Dekker, New York, 1967.

[60] Busuioc, A.O. et al. Quinones in redox flow battery - a study on electrochemical and cyclic behavior of 4 different quinones. Aalborg University Esbjerg Student Report, December 2018.

[61] Ke Xinyou et al. Redox flow batteries with serpentine flow fields: Distributions of electrolyte flow reactant penetration into the porous carbon electrodes and effects on performance. *Journal of Power Sources*, 384:295–302, April 2018.

[62] Newman, J. and Karen E. Thomas-Alyea. *Electrochemical Systems*. Prentice Hall INC., 3 edition, 1973.

[63] Kirchev, A. Battery management and battery diagnostics. In Patrick T. Moseley and Jürgen Garche, editors, *Electrochemical Energy Storage for Renewable Sources and Grid Balancing*, chapter 20, pages 411–435. Elsevier, Radarweg 29, PO Box 211, 1000 AE Amsterdam, Netherlands, 2014.

[64] Zollo, B. Measuring cell capacity. *Electronic Design*, pages 1–3.

[65] Bard, A. J. and Faulkner L. R . *ELECTROCHEMICAL METHODS-Fundamentals and Applications, 2nd ed.* John Wiley & Sons, Inc., 605 Third Avenue, New York, NY 10158-0012,, ii edition, 2001.

[66] Chemistry. `https://opentextbc.ca/chemistry/chapter/17-4-the-nernst-equation/`. e-book from BC-campus, chapter 17, The Nernst Equation.

[67] Kissinger, P.T. and W. R. Heineman. Cyclic voltammetry. *Journal of Chemical Education*, pages 702–706, September 1983.

[68] Milner, D. J. et al. *Analytical Chemistry*, 53:2258, 1981.

[69] Cañizares, P. et al. Measurement of mass-transfer coefficients by an electrochemical technique. *Journal of Chemical Education*, 3(8):1204–1207, August 2006.

[70] Muff, J. et al. Bench-scale study of electrochemical oxidation for on-site treatment of polluted groundwater. *Journal Of Environmental Engineering*, 138:915–922, September 2012. DOI:10.1061/ (ASCE)EE.1943-7870.0000561.

[71] Elgrishi, N. et al. A practical beginner's guide to cyclic voltammetry. *Journal of Chemical Education*, 95:197–206, September 2017. DOI:10.1021/acs.jchemed.7b00361.

[72] Robert Selman, J. and Tobias, C.W. *Mass-Transfer Measurements By The Limiting-Current Technique*, volume 10. Academic Press, Inc, 24/28 Oval Road, London NW1 7DX, 1978.

[73] Chatzisymeon, E. et al. Boron-doped diamond anodic treatment of olive mill wastewaters: Statistical analysis, kinetic modeling and biodegradability. *Water Research*, 43:3999–4009, 2009.

[74] Khasanah, M. et al. The influence of nacl and na2so4 as supporting electrolyte on analysis of lead(ii) in seawater by stripping voltammetry using hanging mercury drop electrode. *Malaysian Journal of Fundamental and Applied Sciences*, 10(3):115–118, September 2014.

[75] La Cerva, M.G. et al. Determination of limiting current density and current efficiency in electrodialysis units. *Desalination*, 445:138–148, July 2018.

6.1 Appendices

This section reports the voltammograms and the values of interest (Table 6.1) of all the quinones analyzed but not chosen for cell cycling.

Table 6.1: Values of peaks position and peak heights.

	$\mathbf{E}_{pa}$	$\mathbf{E}_{pc}$	$\mathbf{i}_{pa}$	$\mathbf{i}_{pc}$
1,8-DHAQ	-0.75684	-0.81543	-0,00099	0.00111
1,5-DHAQ	-0.69092	-0.78369	0,00314	-0,00347
1-HA-9,10-Q	-0.66895	-0.72266	0,00158	-0,00274
1,4-NQ	-0,65918	-0,76172	0,0035084	-0,00414
TF-1,4-BQ	-0,76416	-0,86914	0,0011185	-0,00085696

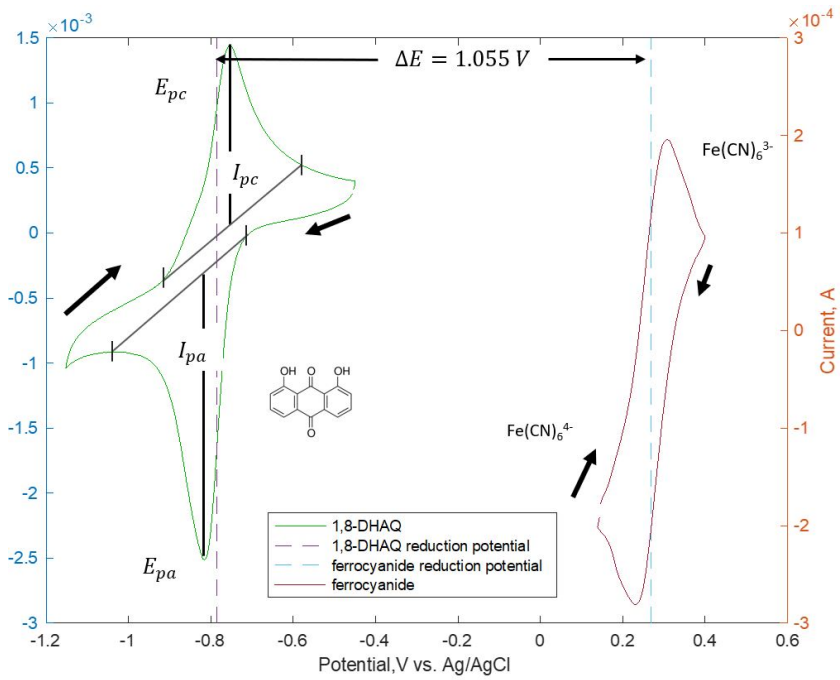

Figure 6.1: Cyclic voltammogram of 2 mM 1,8-DHAQ (green curve) and 10 mM $K_3Fe(CN)_6$ (red curve) in 1 M NaOH, scanned at 500 mV/s. Arrows indicate scan direction.

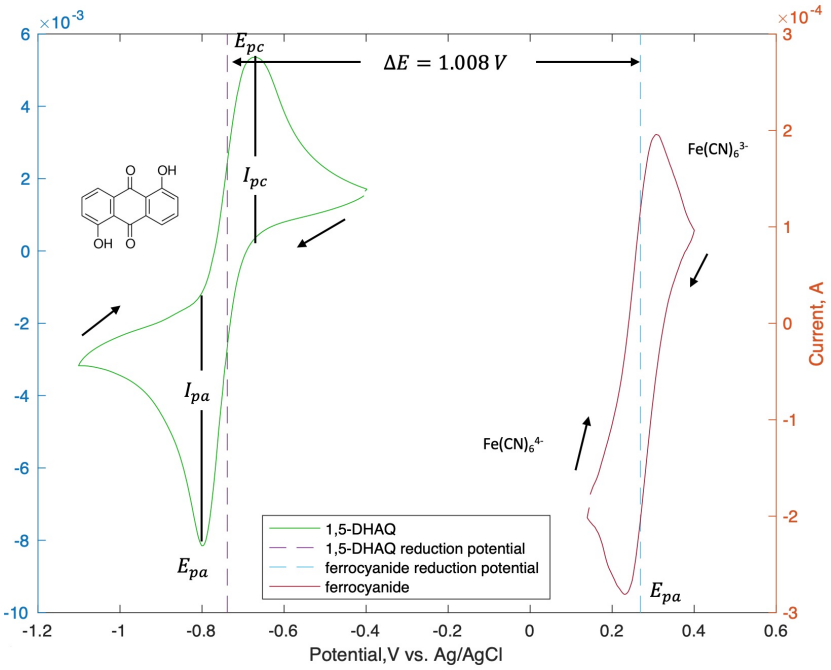

Figure 6.2: Cyclic voltammogram of 10 mM 1,5-DHAQ (green curve) and 10 mM $K_3Fe(CN)_6$ (red curve) in 1 M NaOH, scanned at 500 mV/s. Arrows indicate scan direction.

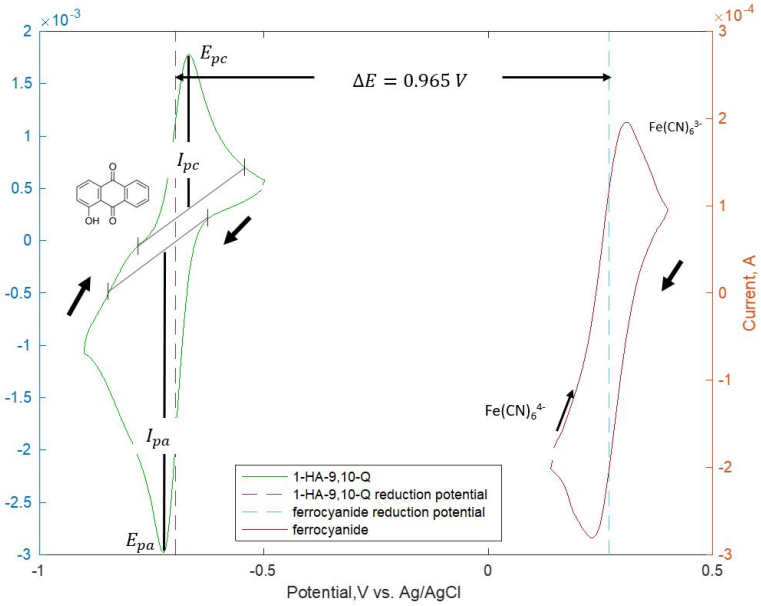

Figure 6.3: Cyclic voltammogram of 10 mM 1-HA-9,10-Q (green curve) and 10 mM $K_3Fe(CN)_6$ (red curve) in 1 M NaOH, scanned at 500 mV/s. Arrows indicate scan direction.

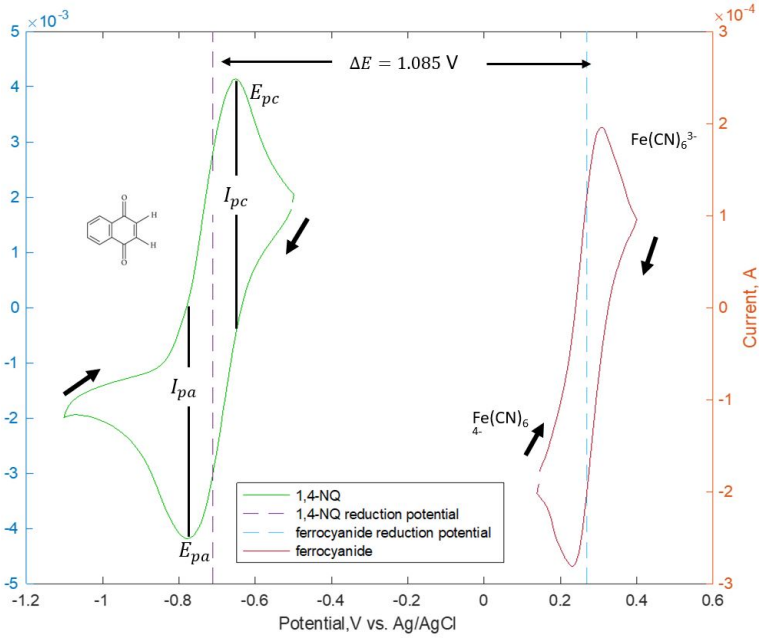

Figure 6.4: Cyclic voltammogram of 10 mM 1,4-NQ (green curve) and 10 mM $K_3Fe(CN)_6$ (red curve) in 1 M NaOH, scanned at 500 mV/s. Arrows indicate scan direction.

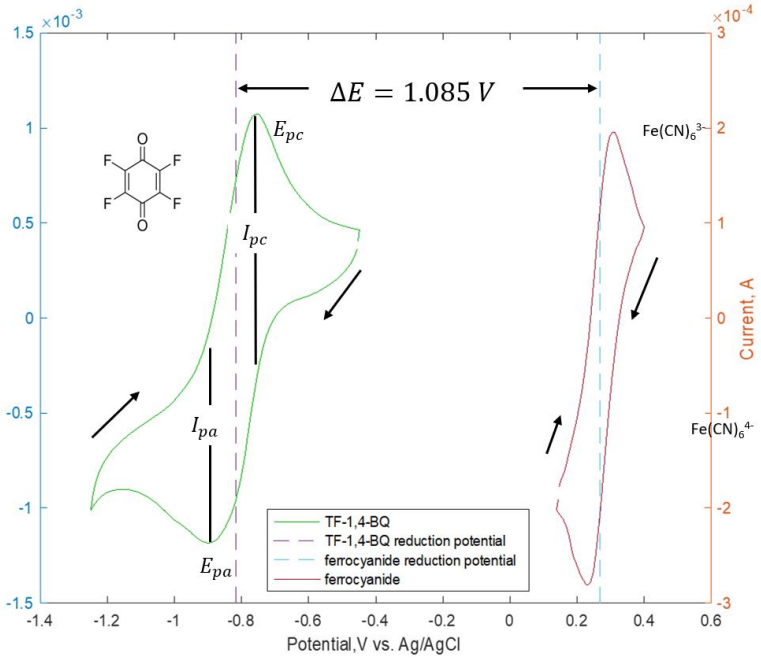

Figure 6.5: Cyclic voltammogram of 10 mM TF-1,4-BQ (green curve) and 10 mM $K_3Fe(CN)_6$ (red curve) in 1 M NaOH, scanned at 500 mV/s. Arrows indicate scan direction.